University of Pavia
PhD Course of Biomedical Science - XXIX Cycle
Coordinator: Prof. Egidio D'Angelo
Department of Brain and Behavioural Science

Two-photon calcium imaging reveals long-term changes in cerebellar granule cell responsiveness following high-frequency mossy fibers stimulation

Doctoral Dissertation by

Marialuisa Tognolina

Supervisor: Prof. Egidio D'Angelo

Academic year 2015-2016

Contents

Declaration

This thesis is submitted to the University of Pavia in support of my application for the degree of Doctor of Philosophy. It has been composed by myself and has not been submitted in any previous application for any degree.

The work presented, including data generated and data analysis, was carried by the author.

Abstract

Recent years have witnessed major improvements in our understanding of the brain thanks to technological developments and a new multidisciplinary approach. Single-cell studies have allowed researchers to gain insights into the detailed characteristics of different neuronal types, while techniques such as functional magnetic resonance imaging (fMRI) enabled an investigation of the global activity of the brain. However, very little is known about the microcircuits function and the way in which each single cell contributes to the final output.

In order to investigate the spatio-temporal organization of neuronal activity in local microcircuits, a simultaneous and fast recording from selected multiple single neurons with a single-cell resolution is required. Optical techniques fit this purpose, but a parallel and fast signal detection requires the presence of multiple confocal excitation volumes that cannot be achieved through traditional confocal and two-photon microscopy. The use of a Spatial Light Modulator (SLM) to divide a coherent excitation light in multiple diffraction limited focal points, which can be configured in different patterns, enabled us to perform optical recordings from different neurons simultaneously. We recently developed an SLM-two photon microscope (SLM-2PM) able to resolve the spatio-temporal organization of activity in acute cerebellar slices through simultaneous calcium signals acquisition from multiple granule cells (GrCs) [1, 2].

In this work the SLM-2PM was optimized to investigate the effect of a mossy fibers (mfs) high-frequency stimulation protocol (HFS), that is known to induce long-term potentiation and depression (LTP and LTD) at the mossy fiber-granule cell (mf-GrC) synapses [3, 4, 5]. After the induction of plasticity we observed long-term changes of

GrCs calcium responses , both as potentiation and as depression (CaR-P and CaR-D), with impressive variations in signal amplitude (CaR-P +317.2 ± 28.7% n=30, CaR-D -66.4 ± 1.6% n=22, 30 minutes after HFS). In particular, CaR-P amplitude changes were several times larger than those reported for synaptic currents measurements [6, 7].

To elucidate the underlying mechanisms we performed patch-clamp experiments in loose cell-attached (LCA) configuration. Also in these experiments, neuronal activity showed prolonged changes comparable to those observed in SLM-2PM recordings.

We then assessed GrCs electroresponsiveness by comparing results from both SLM-2PM and LCA recordings with those previously obtained in our lab through patch-clamp whole-cell recordings (WCRs) and local field potentials measurements [3, 4, 5, 7, 8]. The amplitude changes observed in CaR-P resulted compatible to a combination of changes in GrCs intrinsic excitability and in synaptic transmission leading conjointly to a large increase in the probability of action potential (AP) generation [3].

We performed preliminary SLM-2PM experiments on IB2 KO mice (a recent animal model of autism spectrum disorders) to investigate neurotransmission alterations in the granular layer; SLM-2PM results were in agreement with those from WCRs of our lab (Soda *et al.*, *manuscript in preparation*).

Finally, the comparison between the SLM-2PM and the modeling data sets allowed to validate the network model of the cerebellar granular layer activity developed in our lab.

The results obtained with the SLM-2PM further assess the Ca^{2+} role in the expression of long-term plasticity at the mf-GrC synapses and its critical involvement in determining the sign of plasticity. The consistency of SLM-2PM data with previous results obtained through different techniques indicates that this system can be used to investigate the whole activity of the cerebellar cortex network.

Part I

Introduction

Chapter 1

Cellular network activity

The brain is a network of billions of neurons interconnected in systems which exert centralized control over the other organs of the body. To understand the brain functioning in its entirety, a first step is to learn the individual characteristics of its different neuronal types with their specific features and functionalities. We also need to know how neurons are organized into signaling pathways and how they interact with each other by means of chemical and electrical synapses, giving rise to neuronal circuits in which sensory processes, perception and behavior are built [9, 10].

Each neuron integrates inputs and information from other neurons and it can redistribute this integrated activity back to the neuronal network. During neuronal activity, synapses can experience structural and functional modifications leading to changes in the strength of their connections. This plasticity property is thought to underlie memory and learning [10].

The function of neuronal circuits emerges from complex interactions and coordinated activity among constituents [11]. These networks of neurons exhibit different pattern of activity, including oscillation, synchrony and waves. Recent results in neocortical circuits have also shown that the propagation of spontaneous activity can be described by neuronal avalanches [10, 12, 13].

All these functioning patterns are connected to high-order processes, but their link is yet unknown [13]. Deciphering the exact patterns of brain activity will provide

critical insight not only into healthy conditions but also into what happens when neural circuitry malfunctions in psychiatric and neurological disorders [11, 14].
Although a modeling approach can be used to study the networks activity, the specific mechanisms involved can be reconstructed only on the basis of experimental data. Thus, techniques that allow to monitor the activity of multiple single-cells simultaneously are needed.

1.1 Multiple cells recordings

To investigate the spatio-temporal organization of neuronal activity in local microcircuits, a simultaneous and fast recording from multiple single-cells is required. Optical techniques fit this purpose, but a parallel and fast signals detection requires the presence of multiple confocal excitation volumes that can not be achieved through traditional confocal and two-photon microscopy. In these microscopes, indeed, imaging is typically performed by sequentially scanning a single laser beam across a sample. This results in a low frame rate (i.e. the time required to acquire a complete two-dimensional image of a field-of-view) and in a corresponding poor temporal resolution (usually hundreds of milliseconds), limiting their use in the study of processes with faster kinetics, such as neural activities [15, 16].
In order to develop new technologies able to acquire signals from multiple neurons simultaneously as well as maintaining the single-cell resolution, several approaches taking advantage of computer-controlled and reprogrammable devices have been introduced. These include random access illumination through acousto-optic deflectors (AODs), or targeted path scanning with closed loop scanning mirrors [17]. Although these approaches allow to overcome the traditionally slow raster scanning of confocal and two-photon imaging, the acquired signals are sequential and not completely simultaneous.
On the other hand, the investigation of the activity of a microcircuit and of the contribution of each cell to the final output, requires a perfectly simultaneous acquisition of signals. To this aim, a solution is to split the excitation laser beam into

multiple beamlets that scan the sample in several spatial locations simultaneously. Holographic microscopy, by taking advantage of devices such as diffractive optical elements (DOEs) and digital micromirror devices (DMDs) able to produce arbitrary configurations [18, 19], fit this purpose. However, the patterns obtained with these devices cannot be easily modified.
An alternative solution is to use the spatial light modulators (SLMs). These devices, indeed, allow to divide a coherent excitation light into multiple beamlets which can then be repeatedly configured in different illumination patterns. In this way it is possible to obtain multiple diffraction limited focal points that can be easily directed onto different points in the sample in order to optically record from different points simultaneously [15, 20, 21].

1.2 Cerebellar network

The cerebellar cortex is remarkable for its organization regularity, having a relatively simple and stereotyped connectivity pattern that is identical throughout the whole structure [22, 23, 24] (for a detailed anatomical description of the cerebellum see the appendix).
Figure 1.1 shows a schematic view of the cerebellar network. Two main excitatory pathways convey incoming information to the cerebellum: the mossy fibers (mfs) and the climbing fibers (CFs); from a cellular point of view, only granule cells (GrCs) and unipolar brush cells (UBCs) are excitatory, the other being inhibitory. Mfs contact both GrCs and Golgi cells (GoCs) giving rise to a typical cerebellar structure, i.e. the *glomerulus*. In turn, GrCs axons generate the parallel fibers (PFs) which contact several Purkinje cells (PCs) as well as GoCs. These latter inhibit GrCs through a double feed-forward and feed-back loop. Each PC receives direct excitatory input also from CFs, while basket and stellate cells (BCs and SCs, respectively) inhibit PCs. While PCs provide the sole output from the cerebellar cortex, DCN integrate the PC inhibitory output with the excitatory input carried by mfs and CFs collaterals, giving

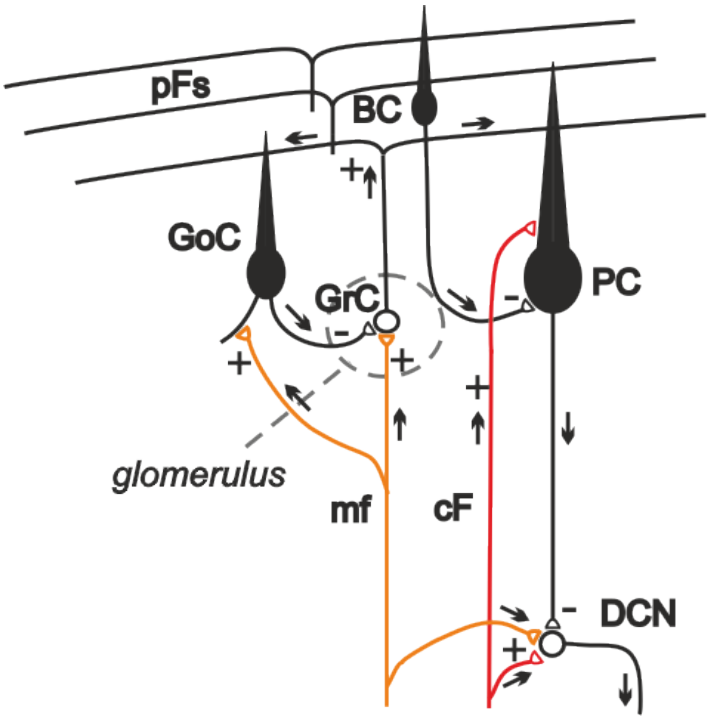

Figure 1.1: *The cerebellar microcircuit.* Schematic sketch of the cerebellar cortex microcircuit. Excitatory inputs are delivered by mfs, CFs and GrCs, while all other neurons are inhibitory. Mfs are the main input of the circuit while PCs axons are the only output of the cerebellar cortex. Adapted from [25].

rise to the sole output of the cerebellum itself [25].

1.2.1 Granular layer functions

The input stage of information in the cerebellar cortex is regulated by the mf-GrC relay. This is characterized by a small convergence and a large divergence according to which each GrC receives a small number of mfs terminals (four to five, as many independent dendrites), while one mf supplies excitatory synapses to 400-600 GrCs in a folium [23, 26, 27]. This convergence/divergence ratio was at the base of the Marr's

theory of the cerebellar cortex learning: the so-called motor learning theory (MLT). In the MLT, the granular layer only performed an operation of pattern discrimination, expansion recoding and gain regulation of the mfs input, while the molecular layer carried out an operation of learning of these informations [28, 29, 30].
Nevertheless, recent experimental evidences show that the granular layer can carry out complex nonlinear spatiotemporal transformations guided by local synaptic plasticity. Long-term synaptic plasticity in the granular layer occurs between mfs and GrCs; it consists of a bidirectional change involving LTP and LTD as well as changes in GrC intrinsic excitability [31]. The expression of LTP and LTD depends on both extrinsic factors (i.e. the input pattern and neuromodulators) as well as on intrinsic factors (i.e. the local inhibitory network activity, which could in turn be regulated and be subject to plasticity). The mfs-GrC plasticity is induced by omosynaptic activity and thus it implements a modality of unsupervised learning; the expression of LTP or LTD depends on the association between mfs activity and postsynaptic depolarization and implements a process of coincidence detection [23].
The granular layer plasticity is thus characterized by timing, geometry and coding properties and it may play a role in regulating cerebellar dynamics, having a critical influence on the selection of mfs patterns to be relayed to the cerebellar cortex [23, 32]. As a whole, the granular layer appears to transform incoming signals and to flexibly control mfs burst transmission for further processing by the PC layer. It behaves as a complex set of filters that operate in time and space domains and that can be adapted through long-term synaptic plasticity [30]. Thus, independent measurements of multiple neurons activity at high temporal resolution are needed to test this hypothesis.

Part II

Chapter 2

Techniques

In this chapter we describe the experimental procedures used and the data analysis performed.

2.1 Slice preparation and solutions

Acute cerebellar slices were obtained from 19 to 24 days old Wistar rats and 129Svev wild type (WT) and knock-out (KO) mice, when GrCs show mature synaptic and excitable properties [33]. Rats and mice were deeply anesthetized with halothane (Aldrich, Milwaukee, WI) and killed by decapitation. Parasagittal (220 μm thick) slices were cut from the cerebellar vermis in cold Krebs' solution containing (in mM): 120 NaCl, 2 KCl, 1.2 $MgSO_4$, 26 $NaHCO_3$, 1.2 KH_2PO_4, 2 $CaCl_2$, 11 Glucose, pH 7.4 when equilibrated with 95% O_2 - 5% CO_2, and then mainteined in Krebs' solution at room temperature for up to 1 hour.
For cerebellar slices bulk loading, a 50 μg aliquot of Fura-2 AM (Molecular Probes, Eugene, OR, USA), previously dissolved in 48 μl of Dimethyl Sulfoxied (DMSO, Sigma Aldrich) and 2 μl Pluronic F-127 (Molecular Probes), was mixed with 2 mL of continuously oxygenated Krebs solution [34, 35]. The slices were then positioned in this solution and maintained at 35°C for 30 minutes in the dark.

Subsequently, the slices were gently positioned in the 2 mL recording chamber of the microscope and fixed with a nylon mesh attached to a platinum Ω-wire to improve tissue adhesion and mechanical stability. Oxygenated Krebs solution maintained at 30°C with a Peltier feedback device (TC-324B, Warner Instruments, Hamden, CT) was perfused (2 mL/min) during the whole experiment.
In all the experiments the GABA-A receptors were blocked by adding 10 μM gabazine (SR95531, Abcam) to the extracellular solution in order to enhance the number of active GrCs during the experiment.

2.2 Two-photon microscopy with SLM-2PM technology

2.2.1 The SLM-2PM

The SLM-2PM is a custom-made upright two-photon microscope that employs a diffractive Liquid Crystal On Silicon-Spatial Light Modulator (LCOS-SLM, X10468-07, Hamamatsu, Japan) both to obtain two-photon images and to collect fluorescence signals. Figure 2.1 shows a schematic view of the system. The laser source that supplies the two-photon excitation is a mode-locked ultrafast Nd:YVO4 Ti:Sapphire laser that generates femtosecond pulses at a repetition rate of 80 MHz, providing 4W maximum power at λ=800 nm (Chameleon Ultra II, Coherent, USA). The laser beam is vertically polarized by a Glan-Taylor polarizer, while a $\lambda/2$ plate is used for power tuning. A 6x telescopic beam expander (f_1= 25 mm, f_2 = 15 mm, Thorlabs Inc. Newton, NJ, USA) collimates and expands the beam in order to optimally fill the LCOS-SLM chip, on which it impinges at 9 deg. The LCOS-SLM chip phase-modulates and reflects the laser beam, while a telescopic beam reducer (f_1= 400 mm, f_2 = 250 mm, Thorlabs Inc. Newton, NJ, USA) is used to reduce the beam to optimally fill the objective back aperture. Finally, a dichroic mirror (750 nm, 750dcspxr, Chroma) directs the beam onto the sample through the objective.

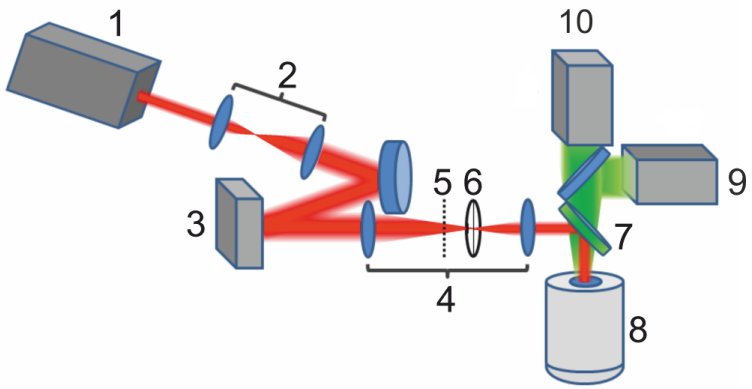

Figure 2.1: *Spatial light modulator-two-photon microscope (SLM-2PM) scheme.* 1. Ti:Sa laser (Chameleon Ultra II, Coherent); 2. beam-expander (f_1= 25 mm, f_2 = 15 mm, Thorlabs Inc.); 3. LCOS-SLM (X10468-07, Hamamatsu); 4. beam reducer (f_1= 400 mm, f_2 = 250 mm, Thorlabs Inc.); 5. illumination pattern formation plane; 6. copper wire for undiffracted light removal; 7. dichroic mirror (750 nm, Chroma); 8. objective (Zeiss Plan-APOCHROMAT 20x 1.0 NA or Zeiss Plan-APOCHROMAT 40x 1.0 NA); 9. CCD camera (CoolSnap HQ); 10. CMOS camera (MICAM Ultima), adapted from [2].

Fluorescence light from the sample is separated from the excitation light through the dichroic mirror, while a flip mirror directs the emission light to a high-spatial resolution CCD camera, for image generation (CoolSnap HQ, Photometrics, Tucson, USA), or to a high-temporal resolution CMOS camera (MICAM Ultima, Scimedia, Japan), for data acquisition. Both the cameras are equipped with a bandpass filter (515/30 nm, Thorlabs Inc. Newton, NJ, USA and 535/22 nm, Thorlabs Inc. Newton, NJ, USA, respectively). Bright-field Köler illumination (not shown) is used to obtain a transmission image of the sample.
A small fraction ($< 25\%$) of the excitation light is not shaped by the SLM (i.e. the "zeroth order" of diffraction). This would produce a bright focal volume at the center of the field of view, generating artifacts on images and inducing photodamage in the sample. To avoid this effect, a copper wire is inserted between the beam reducer lenses in order to avoid this contribution.
Experiments were performed at depths of 50-60 μm, using water-immersion objectives with different magnification (Zeiss Plan-APOCHROMAT 20X 1.0 NA or Zeiss Plan-APOCHROMAT 40X 1.0 NA) [1, 2].

Phase mask calculation

The SLM-2PM is an holographic microscope that takes advantage of the optical Fourier transform properties to obtain any desired configuration of the excitation light on the sample plane. Based on these properties, if a transparent object is placed exactly one focal length in front of a thin lens, the Fourier transform of that object will be formed one focal length behind the lens [36, 37]. Thus, if an electromagnetic field represented by the complex amplitude E_k is placed at the $focal_{front}$ of a lens, the field at $focal_{back}$ will be F_k, where E_k and F_k are Fourier transform pairs (see Figure 2.2, (a)). Thus, to different phase distributions correspond different spatial illumination patterns on the sample plane, as shown in Figure 2.2 (b).

In order to obtain the desired illumination pattern on the sample plane, computed matrices of phase shift values (phase masks) are applied to the incoming laser beam

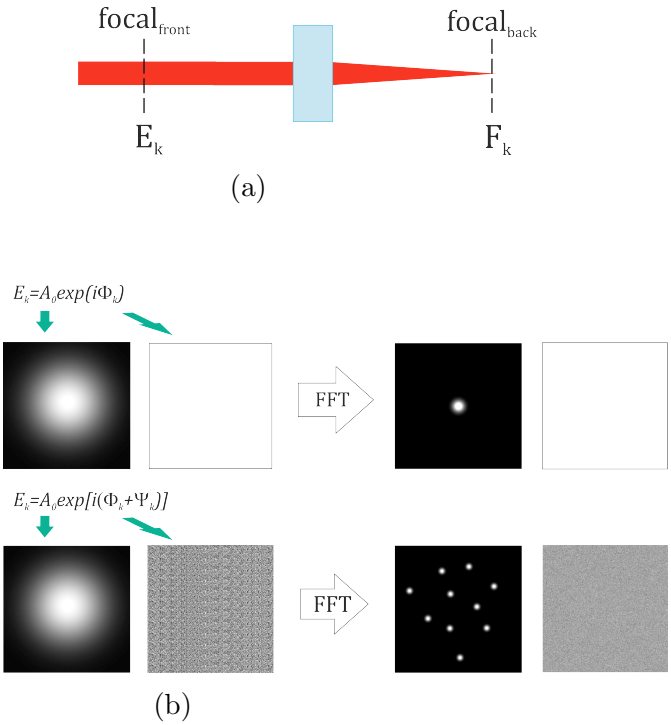

Figure 2.2: *Optical Fourier transform properties.* Based on the optical Fourier transform properties, the Fourier transform of a transparent object placed exactly one focal length in front of a thin lens will be formed one focal length behind the lens. Thus, if the incoming field at focal_{front} is represented by the complex amplitude E_k, the field at focal_{back} will be F_k, where E_k and F_k are Fourier transform pairs (a). Thus, by changing the phase component of E_k, different illumination patterns will be obtained on the sample plane. In (b) an example of different illumination patterns obtained with different phase distributions is shown.

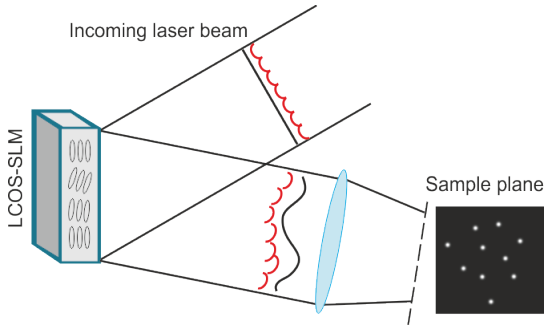

Figure 2.3: *Principle of LCOS-SLM phase modulation.* The LCOS-SLM chip modulates the phase of an incoming light by varying the alignment of its liquid crystals. Each pixel shifts of an arbitrary phase the incoming radiation which is then reflected. Adapted from [38].

through the LCOS-SLM. This computer-controlled reprogrammable device, indeed, by changing the alignment of its liquid crystals, phase modulates the laser beam, as shown in Figure 2.3. It has a 800 x 600 pixel resolution chip, maximum refresh rate of 60 Hz and an encoding phase from 0 to 2π on the beam profile for visible and near infrared light [38].

The phase masks required for the experiments were computed with custom-developed routines written in Python Scipy libraries, based on the classical Fourier transform-based iterative-adaptive Gerchberg-Saxon (GS) algorithm [2, 39, 40]. As shown in the block diagram in Figure 2.4, the algorithm is initialized with the known intensity distribution of the laser beam; an additional user defined phase term is then added, generating E_k. The corresponding Fast Fourier Transform (FFT), F_k, is computed and, preserving the phase information but substituting the calculated amplitude with the target amplitude distribution, the computed image is compared to the desired one. The resulting field is back propagated to the hologram plane by means of an Inverse Fourier Transform (IFFT), and it is modified keeping the phase information but replacing the amplitude distribution with a gaussian one. The algorithm stops after a few iterations, when the argument of the field at the hologram plane converges toward the phase map required to produce the target intensity at the sample plane

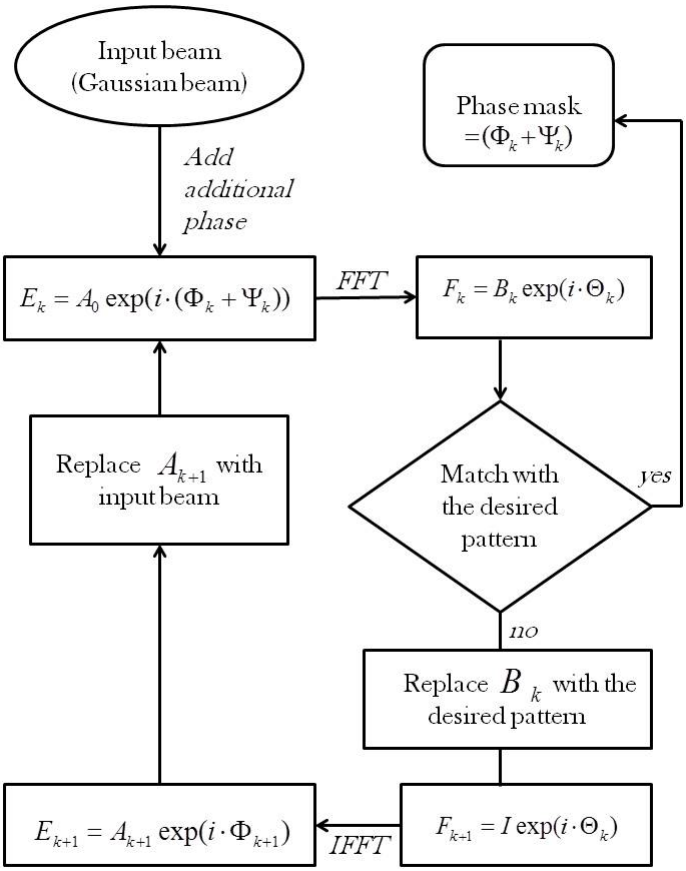

Figure 2.4: *SLM phase mask formation.* Block diagram of the Gerchberg-Saxon-based phase mask algorithm, adapted from [15].

[15].
For the purpose of SLM-2PM microscopy, a phase mask must be computed in a time compatible with experimental needs (seconds); nonetheless, it must be accurate enough to guarantee that every single points of interest (POIs) is illuminated by a diffraction-limited focal volume. Twenty iterations of the algorithm resulted to be sufficient to satisfy both the requirements [2].
Finally, a Fresnel lens pattern is summed to the computed phase mask in order to obtain an image of the desired pattern on a different plane respect to the "zeroth order's" plane, after the first lens of the beam reducer. In this way, the beam-stop used to remove the "zeroth order" contribution does not affect the illumination pattern. Moreover, by changing the focal power of the Fresnel lens summed to the phase mask it is possible to shift the focal plane in the axial direction without changing the objective position, allowing the acquisition of three-dimensional images [2].

Two-photon image acquisition and cell identification

To obtain two-photon images of the sample a sequence of phase mask was computed, each corresponding to a regular square grid pattern (*sliding grid*) of diffraction-limited beamlets (focal points, FPs), as shown in Figure 3.1 (a) and (b). The sequence of this phase mask was calculated so that every point in the *sliding grid* performs a raster scan movement; in this way every beamlet scans a small square area of the sample and elicits fluorescence. Synchronously with the SLM refresh, the CCD camera acquires a stream of images, so that each image frame corresponds to one phase pattern of the sequence (Figure 3.1, (a) and (c)). The CCD camera integrates and stores the fluorescence intensity for every frame and the final image is obtained by assigning to each pixel the fluorescence signal of the corresponding focal point (Figure 3.1, (d)) [2].
The *sliding grid* scan was employed in two different modes: "live imaging mode" and "high-resolution imaging mode", as described below.

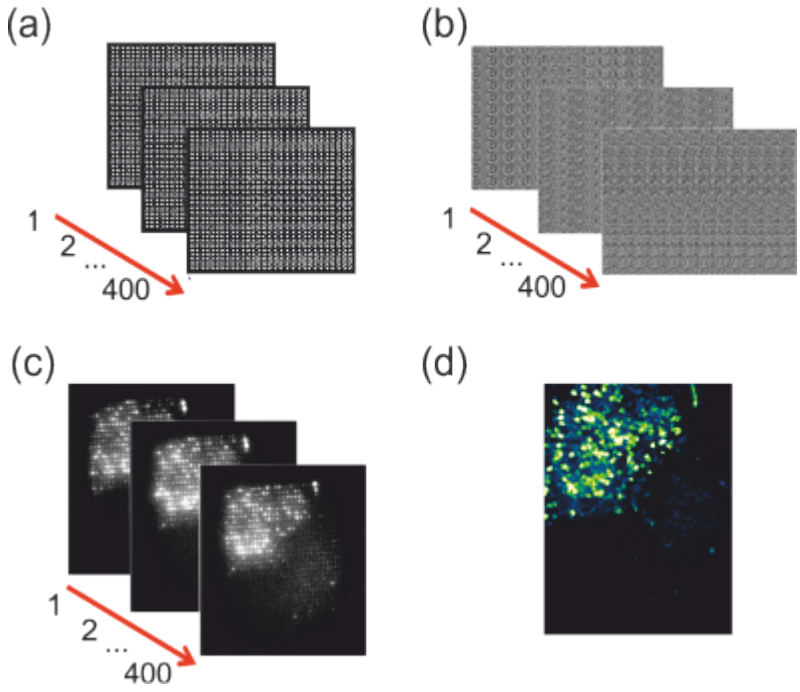

Figure 2.5: *SLM-2PM image acquisition and reconstruction.* A set of regular square grid patterns moving in a raster-scan sequence (a) and of the corresponding holograms (b) was computed. The series of holograms is shown on the LCOS-SLM surface and the resulting wavefront is projected on the sample. The CCD camera acquires an image of the sample for every frame of the sequence and the fluorescence of each FP is stored (c). The fluorescence signals are then converted to grayscale values and assigned to the corresponding pixels of the reconstructed image (d). The figure shows an example of SLM-2PM image acquired with a *sliding grid* of 30 x 30 FPs each moving on a 20 x 20 raster scan pattern, resulting in a sequence of 400 phase masks. The numbers in (a), (b) and (c) indicate the frame index, while the image in (d) was processed offline to highlight GrCs. Adapted from[2].

Live imaging mode Live imaging mode was used for the selection of the fluorescence plane on which measurements should be performed, basing on the number of visible GrCs. Thus, the focal plane with the major number of fluorescence GrCs was set as the plane for the experiment. Since a low resolution confocal image is sufficient to this purpose, a slightly undersampled *sliding grid* (28x28 FPs moving in a 6x6 raster scan pattern) was projected on the sample at the maximum LCOS-SLM refresh rate while the CCD camera exposure time was set equal to an entire sequence duration. Thus, the camera acquires a whole single image, providing a live stream of fluorescence images at about 2 frames per second.

High-resolution imaging mode Once the desired focal plane was identified, we acquired a standard two-photon image of the sample. The software that manage the system allows to choose among different resolutions in which the same image can be acquired by changing the number of FPs and the number of patterns which make up the *sliding grid*. Usually images were obtained using a *sliding grid* made up of 30x30 FPs moving in a 20x20 raster scan pattern, resulting in a sequence of 400 frames acquired by the CCD camera. The field of view covered was of 110x150 μm^2 and of 220x300 μm^2 with 40X and 20X objective, respectively [2].

Multi-spot illumination mode The images obtained using the "high-resolution imaging mode" were used to identify the GrC somata and to select points of interest (POIs) within them. The LCOS-SLM was thus programmed in order to split the laser beam into the required number of beamlets, organized in the desired spatial distribution, thus generating a "multi-spot illumination" pattern (see Figure 2.6 (b)) [1].

For all the acquisition modes, the laser power was set $\leq$ 5 mW/FP.

The experimental procedure thus consisted of different steps:

- we prepare a cerebellar slice and we place it in the recording chamber;
- we select an appropriate region for recordings through bright-field illumination

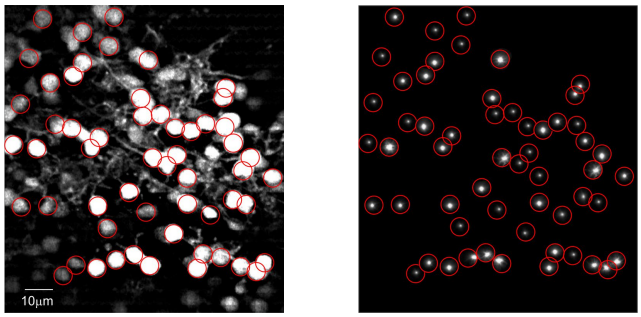

(a) (b)

Figure 2.6: *Fluorescence signals acquisition.* (a) SLM-2PM image of a rat cerebellar slice bulk loaded with Fura-2 AM (50 μg/2mL) acquired with 40X objective. (b) Corresponding "multi-spot illumination" pattern generated by pointing the laser beamlets (bright dots) toward the somata of selected GrCs. Reported from [1].

of the slice;

- we verify the correct staining of the slice in "live imaging mode" and we select the fluorescent plane;
- we acquire a two-photon image of the slice using the "high-resolution imaging mode";
- we used the acquired image to select POIs on different GrCs;
- we generated the phase mask corresponding to the selected POIs positions through the software and the we projected the corresponding "multi-spot illumination" pattern onto the sample;
- we acquired stimulus-induced fluorescence calcium signals through the CMOS camera.

2.3 Stimulation protocols

GrCs activity was elicited by mfs stimulation with a large-tip (10-20 μm) patch-pipette, filled with extracellular Krebs' solution, via a stimulus isolation unit. The same stimulation protocol (10 pulses at 50 Hz repeated 4 times at 0.1 Hz) was applied before and after the delivery of a long-term plasticity induction protocol.
Long-term plasticity was induced using a high-frequency stimulation of the mfs bundle (HFS, 100 pulses at 100 Hz), known to induce long-term potentiation and depression (LTP and LTD) at the mf-GrC synapses, as reported previously [3, 4, 6].

2.4 SLM-2PM recordings and analysis

Fura-2 AM fluorescence signals were acquired from rat and mouse GrC somata through the CMOS camera which was connected through a I/O interface (Brainvision) to a PC controlling illumination, stimulation and data acquisition. The final pixel size was 4.6 x 4.6 μm with 20X objective. Data were acquired at a frequency of 20 Hz and displayed by Brainvision software.
Fura-2 AM fluorescence was excited at 800 nm; at this excitation wavelength the Fura2 isosbestic point is past and therefore any increase in intracellular calcium is observed as a decrease in fluorescence [41, 42]. The mean resting fluorescence, F_0, was sampled for 1400 ms before triggering electrical stimulation. Signals were analyzed off-line as stimulus-induced fluorescence variations normalized to F_0 ($\Delta F/F_0(n) = (F(n) - F_0)/F_0$, where F(n) was the fluorescence intensity at the nth frame). The signal-to-noise ratio (S/N) was improved by averaging 4 consecutive sweeps at 0.1Hz. The analysis was performed by evaluating the peak amplitude (as the difference between signal peak and baseline) of fluorescence signals. Given a peak amplitude of 0.4-0.9 and a noise standard error of about 0.05-0.08, the $\Delta F/F_0$ signal to noise ratio (S/N) was about 8 fold, ensuring a reliable measurement of peak response amplitude. GrCs showed calcium signal variations peaking around 150 ms after the stimulation [1, 2]. The number of active neurons was determined by considering responses larger

than 0.1 $\Delta F/F_0$.
Fluorescence signals were collected before and after the delivery of the HFS protocol, while the number of neurons that showed long-term plasticity was evaluated by considering persistent fluorescence changes over than ±20% after the induction.
Data are reported as mean ± standard error of the mean (S.E.M.) and statistical significance was assessed using paired and unpaired Student's t test (not significant at $p>0.05$).

2.5 Electrophysiological recordings and analysis

Patch-clamp experiments were performed from rat cerebellar unstained slices as well as from Fura-2 AM stained slices (see section 2.1 for details on the staining procedure). Slices were visualized using an upright epifluorescence microscope (Axioskop 2 FS, Zeiss, Germany) equipped with a 5X (MPlan, Olympus, 0.1 NA) or a 40X (LIMPlan FI, Olympus, 0.8 NA) water-immersion objectives, and differential interference contrast (DIC) optics, using infrared illumination (IR, excitation filter 750 nm) and an IR CCD camera (Till Photonics, Germany). Stained slices were identified through a 50W Xe lamp (Zeiss), with excitation and emission filters at 395 nm and 440 nm, respectively. Recordings were obtained with a Multiclamp700B amplifier (3-dB cut-off frequency 10 kHz), and data were sampled with a Digidata 1440A and analyzed off-line with pClamp10 software (Axon Instruments, Molecular Devices, USA).
Patch pipettes were pulled from borosilicate glass capillaries (Hilgenberg, Malsfeld, Germany) and filled with an intracellular solution containing (in mM): 126 K-gluconate, 4 NaCl, 5 Hepes, 15 glucose, 1 $MgSO_4.7H_20$, 0.1 BAPTA-free, 0.05 BAPTA-Ca^{2+}, 3 Mg^{2+}-ATP, 0.1 Na^{+}-GTP, pH 7.2 adjusted with KOH. This solution maintained resting free $[Ca^{2+}]_i$ at 100 nM. Patch pipettes filled with this solution had a resistance of 7-9 MΩ.
The loose cell-attached (LCA) configuration (10-50 MΩ seal resistance) was used to record stimulus-induced GrC action potentials (APs) using the same stimulation protocols as SLM-2PM experiments, in order to elicit the same cellular behavior

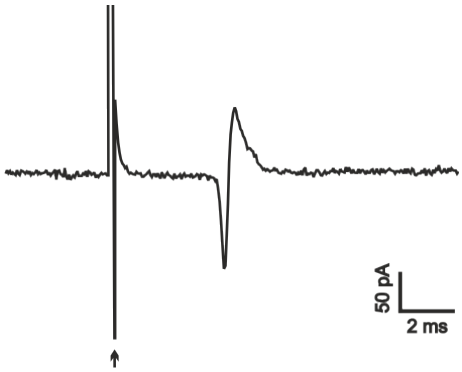

Figure 2.7: *Granule cell action potential in loose cell-attached recordings.* Example of GrC stimulus-induced AP recorded in LCA experiments, showing a biphasic downward and upward deflection. The arrow indicates the mfs stimulus.

(10 pulses at 50 Hz repeated 4 times at 0.1 Hz). In LCA configuration, APs in the recorded cell appear as biphasic, small (20-200 pA peak-to-peak amplitude) current deflections, as shown in Figure 2.7 [43]. Recordings were judged to be stable when (i) the shape and amplitude of spikes were constant over time and (i) the average number of stimulus-induced APs during the stimulation protocol was constant.

In unstained slices there was no need to discriminate between different GrCs, so blind patch clamp method was used to record GrCs activity. In bulk loaded slices, instead, it was necessary to identify the dye-filled neurons, thus in this case GrCs were visually target.

Neuronal activity was analyzed off-line as number of stimulus-induced APs. The analysis was performed by evaluating the average number of APs evoked at each acquisition, before and after the delivery of the HFS protocol. Long-term plasticity was evaluated by considering statistically significant changes in the average number of APs after the plasticity induction.

Data are reported as mean ± standard error of the mean (S.E.M.) and statistical significance was assessed using paired and unpaired Student's t test (not significant at $p>0.05$).

Ethical statement All experiments were conducted in accordance with international guidelines on the ethical use of animals (European Union Directive 2010/63/EU), and approved by the local ethical committee of the University of Pavia.

Chapter 3

Previous experimental results

In this chapter, we briefly summarize previous results obtained with the SLM-2PM with the aim to highlight the features of the system and to set the logical path of the subsequent experiments[1].

3.1 SLM-2PM microscopy

The SLM-2PM was used to acquire two-photon fluorescence images of rat cerebellar slices bulk loaded with Fura-2 AM (for details see Chapter 2), both using a 40X or a 20X objective (examples of which are shown in Figure 3.1). The acquired images were used to identified GrCs for subsequent fluorescence calcium signals recordings. Thus, a crucial point was to determine the system accuracy in terms of resolution and pointing preciseness. For this purpose, we acquired images of a sample of under-resolved fluorescent polystyrene beads (100 nm diameter) immobilized in agarose gel and we made pointing trials. Lateral and axial resolutions obtained were of 420 ± 6 nm and 1.15 ± 0.08 μm, respectively, in agreement with theoretical values; POIs selection accuracy resulted higher than half of the focal volume dimension (200

[1] A more detailed discussion of the results summarized here can be found in [1], where my main contribution was in the execution of the experiments.

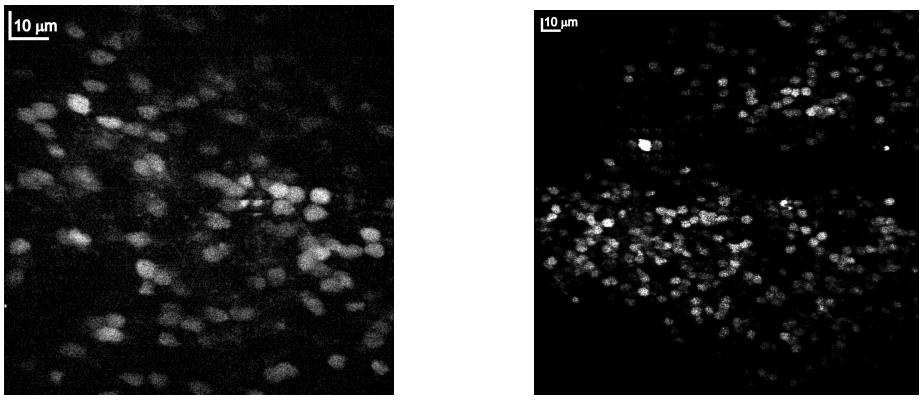

(a) (b)

Figure 3.1: *Examples of SLM-2PM images.* SLM-2PM images of rat cerebellar slices bulk loaded with Fura-2 AM (50 μg/2mL). Several GrCs are visible in both the images, which were acquired with a 40X and a 20X objective, (a) and (b), respectively.

nm for 1.0 NA objectives). Thus, the system proved to be diffraction limited and demonstrated an image generation efficiency comparable to conventional two-photon microscopes [1, 2].

3.2 Calcium signals from multiple neurons

The SLM-2PM was used to investigate the neuronal activity by recording calcium signals from multiple single GrCs simultaneously. To this aim, an image of the granular layer was acquired (for details on the acquisition modes, see Chapter 2) and GrCs for the subsequent activity recordings were identified. An arbitrary illumination pattern was thus generated through the "multi-spot illumination" procedure and the stimulus-induced fluorescence signals in response to mfs stimulation (10 pulses at 50 Hz) were collected.

The Figure 3.2 shows an example of multiple calcium signals acquisition: on the left a SLM-2PM reconstructed image of the granular layer with the user selected POIs is

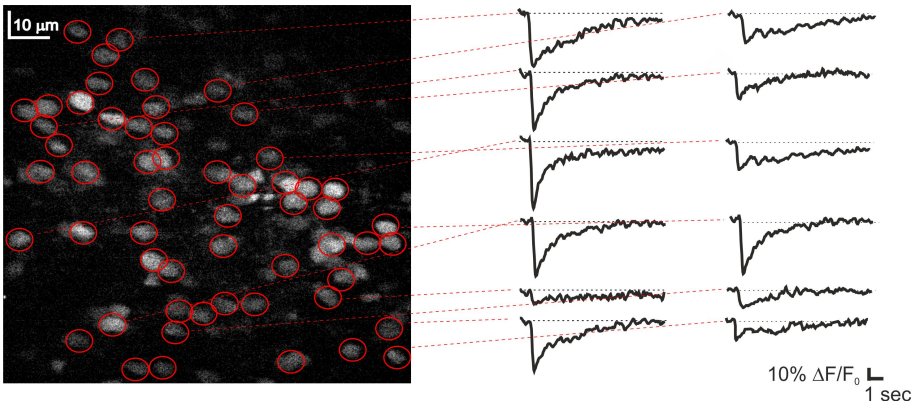

Figure 3.2: *Simultaneous calcium signals acquisition from multiple GrCs through the SLM-2PM.* Left: SML-2PM image generated by Fura-2 AM bulk loading (50 μg/2mL) of a rat cerebellar slice; right: examples of stimulus-induced Ca^{2+} signals detected from the soma of GrCs in response to mfs stimulation (10 pulses at 50 Hz). Fura-2 AM fluorescence signals appear as $\Delta F/F_0$ reduction induced by intracellular calcium increase. Adapted from [1].

reported, while calcium transients acquired simultaneously from multiple GrCs are shown on the right.

3.3 Nature and features of calcium signals

Fluorescence calcium signals were recorded as $\Delta F/F_0$ variations elicited by mfs stimulation (10 pulses at 50 Hz). Their nature was assessed by evaluating the effect of selective synaptic receptor antagonist on (i) the $\Delta F/F_0$ peak amplitude and on (ii) the number of active cells. These two parameters were evaluated both in control condition, with extracellular Krebs' perfusion, and during the perfusion of a solution containing the GABA-A receptor blocker gabazine (20 μM). After gabazine perfusion the values of both the parameters analyzed increased (+129.9 $\pm$ 2.5%, n = 15 slices, $p < 0.001$ and +89.1 $\pm$ 11.3%, n = 15 slices, $p < 0.01$, respectively). Subsequently a solution containing NMDA glutamate receptor blocker (D-APV, Abcam, 50 μM)

was perfused; this markedly reduced both the peak amplitude and the number of active cells (-75.5 ± 12.3%, n = 6 slices, $p < 0.01$ and -79.6 ± 9.3%, n = 6 slices, $p < 0.01$, respectively). Finally, the application of an AMPA glutamate receptor blocker (NBQX, Abcam, 10 μM) completely blocked the residual GrCs activity (-100%, n = 5 slices, $p < 0.01$).

The figure 3.3 depicts the time courses of $\Delta F/F_0$ peak amplitude and of the number of active cells. As shown, both the parameters were modulated by the effect of the synaptic receptors blockers, demonstrating the synaptic origin of calcium signals as consequent to the glutamate receptors activation [1].

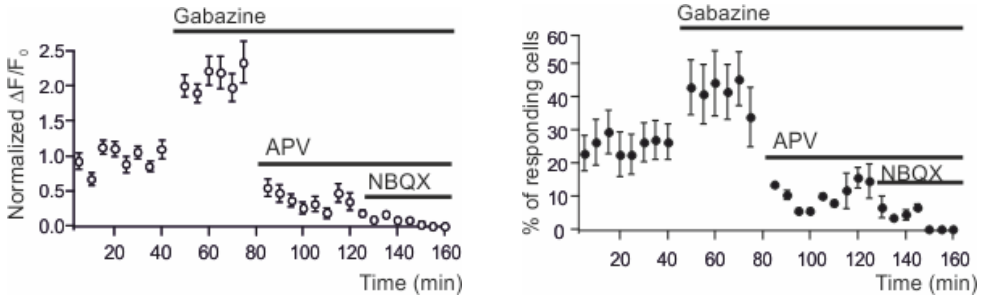

(a) (b)

Figure 3.3: *Regulation of GrCs activity by synaptic receptor blockers.* Time courses of (a) the normalized $\Delta F/F_0$ peak amplitude and of (b) the number of responding GrCs following the application of selective synaptic blockers. The synaptic origin of SLM-2PM calcium signals was assessed as due to the glutamate receptors activation. Reported from [1]

To determine the relationship between $\Delta F/F_0$ signals and neuronal electroresponsiveness whole-cell patch-clamp recordings (WCRs) with 200 μM Fura-2 in the patch-pipette were performed from GrCs. The relationship between $\Delta F/F_0$ and the number of GrC spikes was evaluated during repetitive mfs stimulation (20 stimuli at 100 Hz). Voltage traces showed EPSP-spike complexes correlated with sustained calcium transient, as shown in Figure 3.4 (a). The number of spikes generated by

GrCs in response to the mfs stimulation was variable, probably reflecting quantal variability in the neurotransmission process [7]. Nevertheless, it was possible to assess a quasi-linear correlation between (i) the number of GrC spikes and the $\Delta F/F_0$ peak amplitude ($R^2 = 0.85$, $p < 0.05$, $n = 5$), as well as between (ii) the number of GrC spikes and the time required by the fluorescence signals to reach their peak amplitude (time-to-peak, $R^2 = 0.94$, $p < 0.01$, $n = 5$), as shown in Figure 3.4 [1].

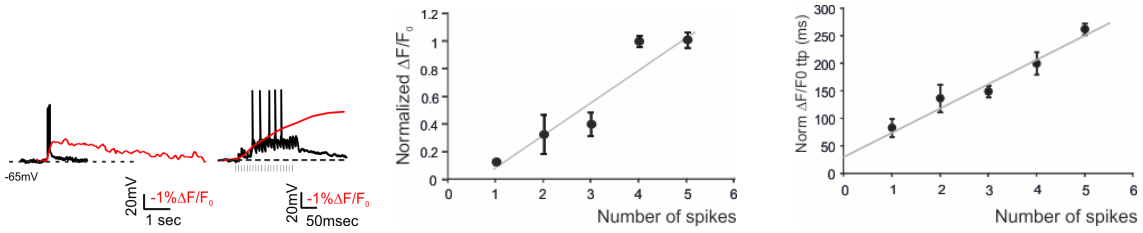

(a) (b) (c)

Figure 3.4: *The relationship between GrCs activity and calcium signals.* (a) Repetitive mfs stimulation (20 stimuli at 100 Hz) induced EPSP-spike complexes correlated with calcium transient in GrCs. (b) Dependence of normalized $\Delta F/F_0$ peak and (c) of normalized $\Delta F/F_0$ time-to-peak on the number of spikes emitted by GrCs in response to mfs bursts, showing a quasi-linear correlation. Reported from [1].

3.4 Signals stability

Signals stability was verified by repetitively stimulating the mfs (10 pulses at 50 Hz) at 0.1 Hz and monitoring (i) the $\Delta F/F_0$ peak amplitude and (ii) the number of responsive GrCs. Both these parameters showed a remarkable stability over 2 hours (-0.1 and -1% decrease, respectively, as shown in Figure 3.5). This probably reflected the low light intensity of the beamlets (3-5 mW/μm^2) and the small area covered over the cells, which could limit the photobleaching and the production of toxic metabolites [1].

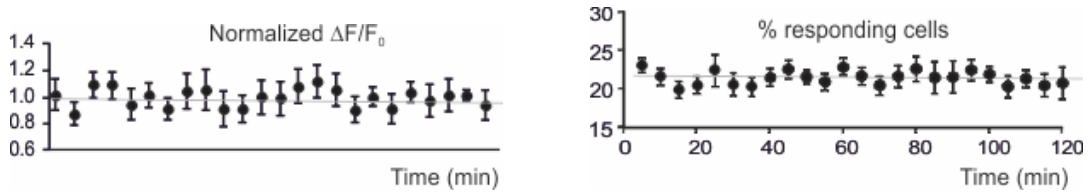

(a) (b)

Figure 3.5: *SLM-2PM calcium signals show a remarkable temporal stability.* (a) Time courses of $\Delta F/F_0$ calcium signals and (b) of the average number of active GrCs (b) in response to mfs burst stimulation (10 pulses at 50 Hz repeated at 0.1 Hz), average from 54 GrCs in three experiments. Note signal stability over 2 hours of recordings. Reported from [1].

3.5 Organization of the granular layer activity

The single-cell resolution achievable with the SLM-2PM was used to characterize the spatial organization of the granular layer activity. For this purpose, GrCs calcium signals elicited by mfs stimulation (10 pulses at 50 Hz) were acquired both in control condition and after the GABA-A receptor blocker (20 μM gabazine) perfusion; the corresponding activity maps were then reconstructed.

In control condition, a spot of active GrCs emerged, while a larger active area with stronger activation intensity was observed after gabazine perfusion (n = 5 slices, Figure 3.6 (a) and (b), respectively). In order to visualize the effect of inhibition in regulating granular layer activity, an excitatory/inhibitory balance map was generated ("E/I" map, E/I = (E_{norm}-I_{norm})/E_{norm}, where E_{norm} is the response intensity normalized to maximum response and I_{norm} is the response variation following gabazine perfusion normalized to the maximum). A center-surround structure, characteristic of the granular layer activity, emerged, as shown in Figure 3.6 (c) [1].

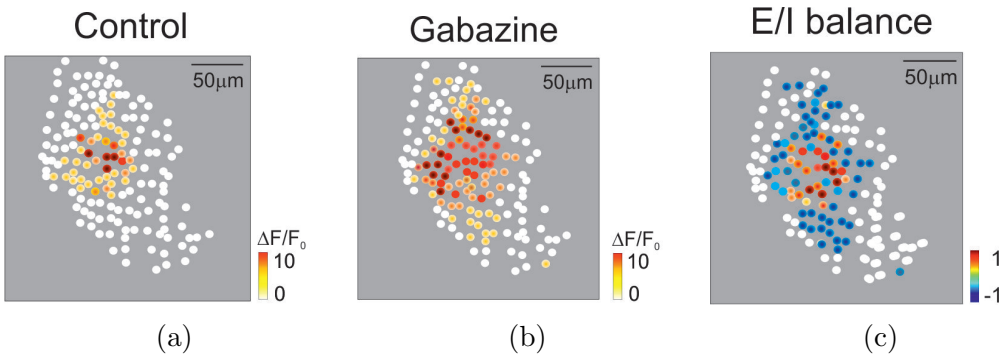

(a) (b) (c)

Figure 3.6: *Spatial organization of the granular layer activity.* Activity maps of the peak intensity of neuronal responses on a color scale, in control condition and during gabazine perfusion, (a) and (b), respectively. In (c) the excitatory/inhibitory (E/I) balance plot is shown: the excitation prevails in the core while inhibition exceeds excitation in the surround. The location of colored dots corresponds to that of neurons in the slice. Reported from [1].

.

Chapter 4

Experimental results

Previous experimental results (briefly summarized in chapter 3) proved that the SLM-2PM can be used to perform calcium imaging recordings. These experiments assessed the synaptic origin of the calcium signals (as due to the glutamate receptors activation) and their correlation with the neuronal electroresponsiveness. Moreover, a remarkable temporal stability of the fluorescence signals was demonstrated.
However, it was unclear whether the SLM-2PM could be used to study changes in synaptic transmission. Thus, in this work, we used the SLM-2PM to perform prolonged experiments in order to study long-term plasticity in the cerebellar granular layer.

4.1 Calcium-Related plasticity (CaR-P and CaR-D)

In order to test whether it was possible to investigate long-term plasticity as persistent variations in calcium signals, we performed long-term plasticity experiments with the SLM-2PM both on rat and on IB2 WT mouse cerebellar slices.

Stimulus-induced calcium signals from multiple GrCs were simultaneously acquired for a control period of about fifteen minutes (see section 2.3 for details on stimulation protocols) to ensure signal stability. Long-term plasticity was induced through a HFS protocol delivered to the mfs bundle; then, calcium signals were recorded for at least twenty minutes after the induction, through the same stimulation protocol used in control condition.

Following the HFS protocol, we observed persistent variations of the amplitude of GrCs calcium signals, both in the recordings from rat slices and in those from mouse slices. The variations occurred as calcium-related long-term potentiation (CaR-P) as well as calcium-related long-term depression (CaR-D). The $\Delta F/F_0$ peak amplitude of calcium signals showing CaR-P increased by $+388 \pm 34.3\%$ for GrCs from rat slices and by $+309.2 \pm 24.3\%$ for GrCs from mouse slices, as reported in Figure 4.1 (a) ($n = 17$ and $n = 13$, respectively, 30 min after HFS, $p < 0.005$ for both). GrCs showing CaR-D decreased their calcium signals by $-73.8 \pm 2.5\%$ and by $-61.9 \pm 2.2\%$ for rat and mouse slices recordings, respectively ($n = 4$ and $n = 18$, respectively, 25 min after HFS, $p < 0.001$ for both, Figure 4.1 (b)). GrCs that did not show significant changes after HFS were also observed ($-7.4 \pm 6.2\%$, $n = 5$ for rat slices and $-5.9 \pm 3.7\%$, $n = 5$ for mouse slices), as reported in Figure 4.1 (c). Interestingly, CaR-P and CaR-D showed a biphasic increase (or decrease, respectively) in the calcium signals, consisting of a rapid phase followed by a second one that peaks around 30 minutes after the HFS.

Figure 4.1 (d) and (e) shows the incidence histograms of CaR-P, CaR-D and no change for rat and mouse GrCs, respectively (CaR-P: 65.38%, CaR-D: 15.38%, no change: 19.24% for rat GrCs and CaR-P: 36.11%, CaR-D: 50%, no change: 13.89% for mouse GrCs). No significant differences were found between rat and mouse GrCs for the different trends observed ($p = 0.69$ for LTP, $p = 0.29$ for LTD, $p = 0.59$ for no change), so data from the two distinct species were averaged together and normalized. Figure 4.2 shows the relative time course.

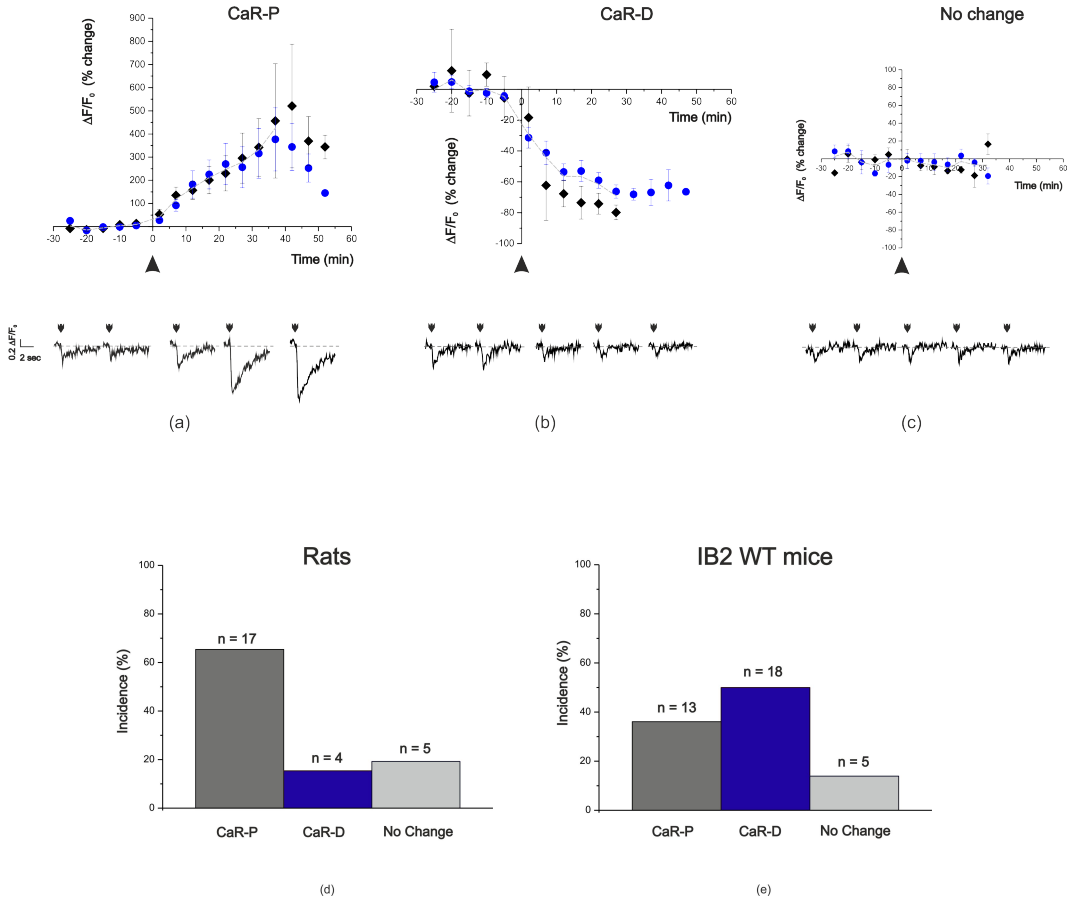

Figure 4.1: *The SLM-2PM reveals calcium-related long-term plasticity.* A HFS plasticity protocol delivered to the mfs bundle induced persistent variations in GrCs calcium signals amplitude from rat (♦) and mouse (•) cerebellar slices, both as potentiation (CaR-P, shown in (a)) and as depression (CaR-D, shown in (b)). In (c) the time courses of rat and mouse GrCs showing no changes in their signals amplitude are reported. The values obtained by averaging rat and mouse GrCs data are reported in (a), (b) and (c) as dotted lines. Bottom traces are example of stimulus-induced calcium signals acquired before and after the HFS, for the different trends. In this and in the following figures the HFS is indicated by an arrowhead; data points are reported as mean ± s.e.m.
Incidence histograms of CaR-P, CaR-D and no change for rat and mouse GrCs are shown in (d) and (e), respectively.

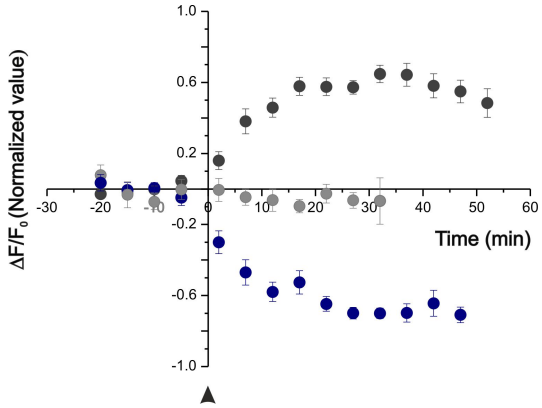

Figure 4.2: *Calcium-related long-term plasticity in rat and mouse GrCs.* Since no significant differences were found between rat and mouse GrCs for the different trends observed, the data were averaged together and normalized. This graph shows the time course corresponding to CaR-P, CaR-D and no change trends simultaneously. The arrowhead indicates the HFS; data points are reported as mean ± s.e.m.

4.1.1 The nature of CaR-P

CaR-P showed an impressive percentage increase in calcium signal amplitude, notably larger compared to that reported for LTP of synaptic currents [6, 7]. In order to unravel the nature of this discrepancy, we compared our data to pre-existing electrophysiological investigations of LTP in the same cells.

Using WCRs measurements, a three-fold increase of GrC intrinsic excitability was observed after a protocol of plasticity induction [3]. Basing on the established quasi-linear correlation between the number of GrC emitted spikes and the SLM-2PM calcium signals (see section 3.3 for details), we computed the $\Delta F/F_0$ changes due to a three-fold increase in the number of APs emitted. The resulting 316% increase in the $\Delta F/F_0$ signal proved to be in good agreement with the average CaR-P values observed of $+326.7 \pm 21.2\%$ (n = 27, average value calculated between 15 to 52 minutes after HFS). The good correspondence between these values suggests that the CaR-P increase partly reflects a change in the number of GrC emitted APs.

The upper panels of Figure 4.3 show, from the left, the time course of the GrC probability of firing before and after the induction of plasticity, reported from [3], and the quasi-linear correlation between the number of spikes and $\Delta F/F_0$, adapted from [1]. In Figure 4.3 (c) and (d) the time courses of normalized $\Delta F/F_0$ and of the corresponding $\Delta F/F_0$ percent change of GrC CaR-P are shown, respectively.

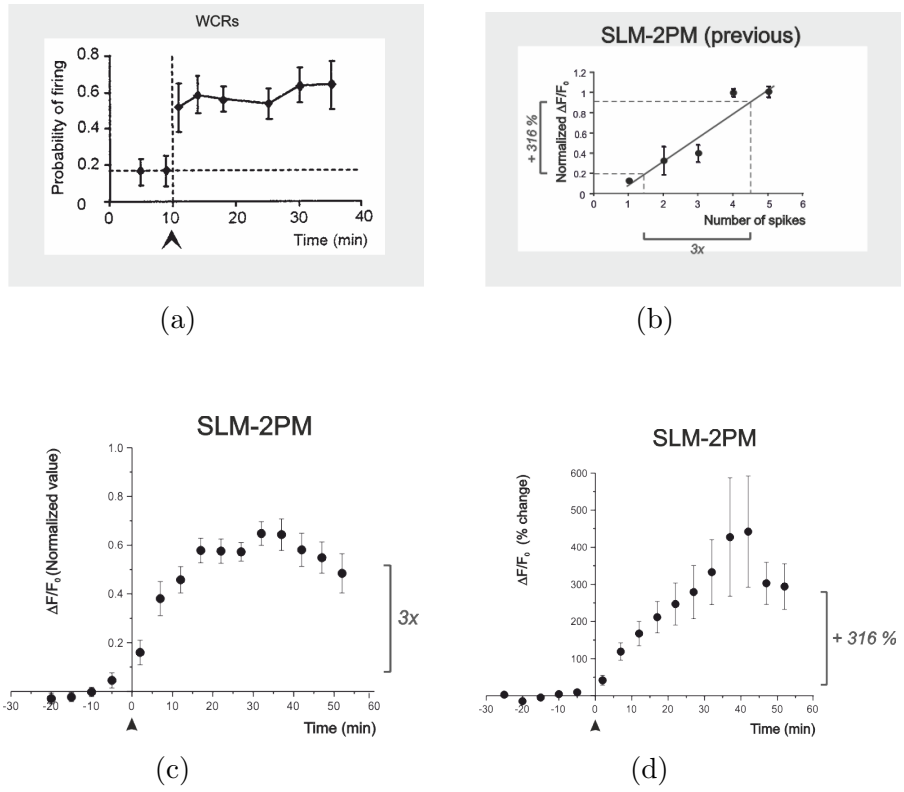

Figure 4.3: *The nature of CaR-P.* (a) Time course of the probability of firing before and after plasticity induction at the mf-GrC synapse, reported from [3]. (b) Correlation between the number of GrCs spikes and the normalized $\Delta F/F_0$ signals, adapted from [1]. We computed the $\Delta F/F_0$ percentage increase corresponding to a 3x increase in the number of emitted spikes. According to prediction, the observed CaR-P percent change corresponds to a three-fold increase in the number of emitted APs, as shown by the time courses of the normalized $\Delta F/F_0$ and of the $\Delta F/F_0$ percent change of the CaR-P reported in (c) and (d), respectively.

4.2 Loose cell-attached measurements

In order to investigate the neuronal activity changes underlying the CaR-P and CaR-D observed with the SLM-2PM and to validate these results, we performed patch-clamp experiments in LCA configuration both on unstained rat cerebellar slices and on rat slices stained with Fura-2 AM (see sections 2.1 and 2.5 for details on the slices preparation and on the electrophysiological recordings). Similarly to SLM-2PM experiments, we acquired stimulus-induced APs from GrC before and after the induction of plasticity, using the same stimulation protocols applied in SLM-2PM measurements (see section 2.3 for details on the stimulation protocols).

In both unstained and stained slices, we observed temporal trends similar to those reported in calcium imaging experiments. The number of emitted GrC APs showed long-term variations after the HFS protocol, both as an increase and as a decrease of the number of stimulus-induced APs (APs-P and APs-D, respectively), while some cells did not show significant changes after the induction protocol.

Figure 4.4 depicts the percent changes observed in GrCs from both unstained and stained slices, categorized by the post induction trend of GrC activity (for unstained slices: APs-P $+176.2 \pm 25.1\%$, n = 10; APs-D $-54.0 \pm 3.8\%$, n = 5; no change $-4.8 \pm 3.7\%$, n = 5; for stained slices: APs-P $+85.4 \pm 6.7\%$, n = 10; APs-D $-73.9 \pm 2.9\%$, n = 7; no change $-0.4 \pm 5.3\%$, n = 5).

No significant differences were found between unstained and stained slices for the different trends observed (p = 0.44 for APs-P, p = 0.23 for APs-D, p = 0.61 for no change). However, in the APs-P time course it can be observed a variability in the percentage values reported. Rather than due to a physiological difference between unstained and stained slices, this is likely related to a different cellular sampling, as discussed further below.

Figure 4.5 (a) and (b) shows the normalized time courses relative to GrC activity recorded from unstained and stained slices, respectively, while (c) and (d) shows

incidence histograms of APs-P, APs-D and no change behaviors of GrC activity, for the two conditions (unstained slices: APs-P 50%, APs-D 25%, no change 25%; stained slices: APs-P 45.45%, APs-D 31.81%, no change 22.72%). The major incidence of APs-P over APs-D and no change reflects the condition of blockage of inhibition (i.e. gabazine perfusion) maintained during the experiments.

4.3 Comparison with whole-cell measurements

We compared results obtained from LCA long-term plasticity experiments with those reported from previous WCRs in order to verify whether the GrCs' features previously observed were confirmed.

Sola *et al.* investigated the mechanism of LTP generation in GrCs, describing the relationship between the probability (p) of quantum release and LTP magnitude [7]. The p change and the intensity of LTP resulted to be negatively correlated with the initial p value, so that GrCs showing low initial p value underwent a higher percent increase after LTP induction, as shown in Figure 4.6 (a).

In GrCs the occurrence of an AP is positively correlated to the presynaptic probability of release; in particular, an AP elicited by a single mfs stimulus is related to a high p value.

Based on this consideration, we investigated whether a relationship similar to that observed in Sola *et al.* could be inferred from our experiments. To this aim, we calculated the average probability that the first pulse of each sweep of the stimulation protocol elicits an AP during the control period. This value was then correlated with the magnitude of the potentiation observed.

A linear correlation between these two parameters could be inferred, both in recordings from unstained and stained slices. Figure 4.6 (b) and (c) depicts these relationships, respectively. As mentioned in the previous paragraph, no significant differences were

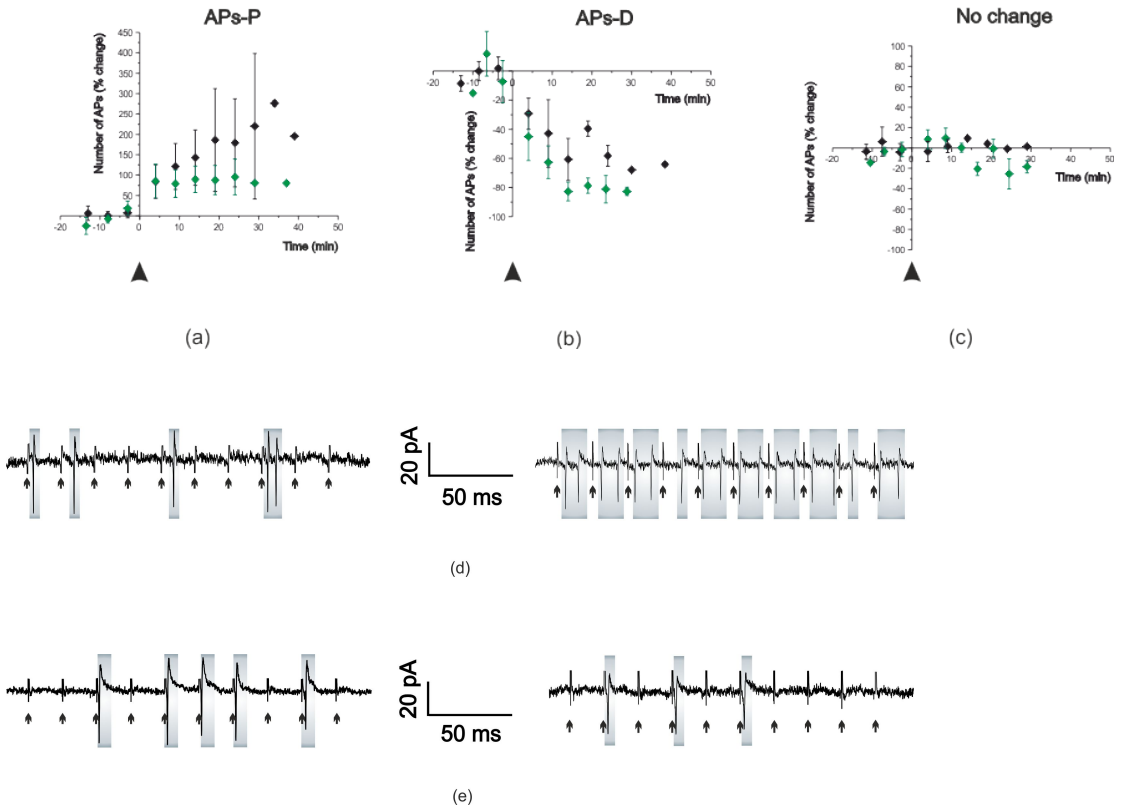

Figure 4.4: *LCA recordings reveal properties similar to SLM-2PM measurements.* In (a), (b) and (c) the time courses of GrC activity recorded from unstained (♦) and stained (♦) slices are shown for APs-P, APs-D and no change behavior, respectively. Every points of the time courses is the result of a 5 minutes bin width. In this and the following figures, an arrowhead indicate HFS; data points are reported as mean ± s.e.m.
In (d) and (e) examples of LCA traces acquired before and after the HFS are reported for GrCs showing APs-P and APs-D, respectively. As it can be noted, GrCs that underwent APs-P increased both the number and the frequency of APs, while the opposite occurs for APs-D.

found between unstained and stained slices and indeed, except for one point, the two distributions showed a similar trend (unstained slices: $r^2 = 0.73$, $p < 0.005$, F-test, $n = 10$; stained slices: $r^2 = 0.45$, $p < 0.05$, F-test, $n = 10$).

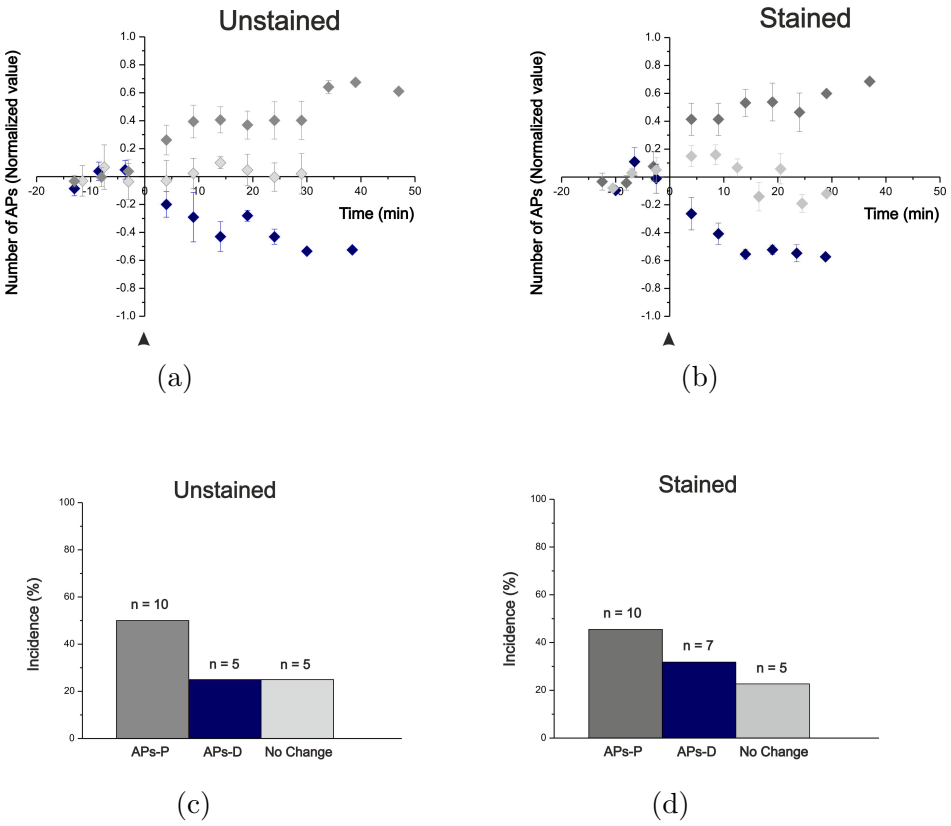

Figure 4.5: *LCA recordings reveal long-term plasticity in GrCs activity recorded from unstained and stained slices.* GrC activity revealed both APs-P, APs-D and no change behaviors after the induction protocol, both in unstained and in stained rat cerebellar slices. To visualize the different trends simultaneously, the relative normalized time courses are shown in (a) and (b), for unstained and stained slices, respectively. Incidence histograms for APs-P, APs-D and no change are shown in (c) and (d) for unstained and stained slices, respectively.

Gall *et al.* and D'Errico *et al.* investigated the effect of different mfs bursts on synaptic plasticity by varying the mfs burst duration while maintaining a fixed frequency of stimulation, [4], and by varying the frequency stimulation while maintaining the same number of pulses, [5], respectively. The relationships between $[Ca^{2+}]_i$ and plasticity

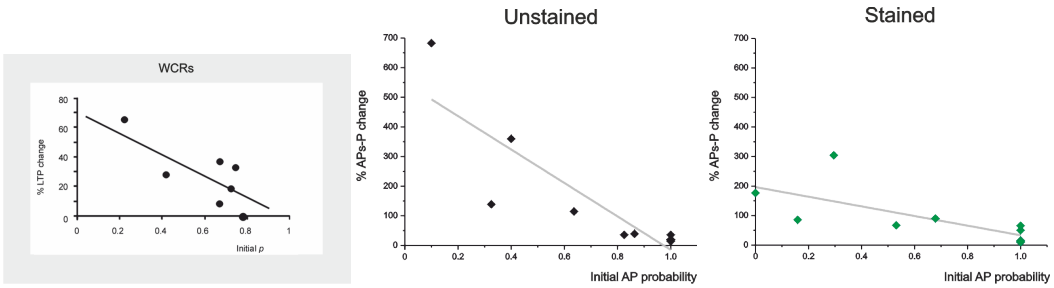

(a) (b) (c)

Figure 4.6: *The relationship between the probability of quantum release and LTP magnitude.* In (a) the indirect relationship between the initial p values and LTP magnitude observed through WCRs is shown (reported from [7]). The correlations between the probability of AP generation in response to a single mfs stimulus and the magnitude of the potentiation reached for recordings from unstained and stained slices, are shown in (b) and (c), respectively. Also in LCA recordings the parameters showed a negative correlation.

were established and revealed a curve resembling the Bienenstock-Cooper-Munro (BCM) learning rule [44] and a U-shape curve, respectively. These two relationships resemble one each other, showing LTD for low $[Ca^{2+}]_i$, a neutral point for moderate $[Ca^{2+}]_i$, and LTP at relatively high $[Ca^{2+}]_i$, as shown in Figure 4.7 (a).

In order to assess whether a similar relationship could be inferred from LCA experiments, we correlated the number of APs occurring during the HFS protocol with the post induction trend observed. GrCs that emitted a low number of spikes (as respect to the number of stimuli) during the HFS underwent APs-D, GrCs that responded to the HFS with a medium number of spikes showed no change, while GrCs that emitted a high number of spikes (the same or more respect to the number of stimuli) resulted in APs-P. The corresponding relationship revealed a U-shape curve similar to that observed in [5], both for unstained and stained slices, as shown in Figure 4.7 (b) (average number of spikes emitted during HFS and average percent change after HFS for unstained slices: 25.6 ± 10.3 and $-53.2 \pm 11.6\%$ for APs-D, 50.8 ± 20.6 and $-4.5 \pm 4.7\%$ for no change, 72.2 ± 11.9 and $145.8 \pm 68.3\%$ for APs-P; for stained slices: 23.3 ± 11.2 and $-67.9 \pm 5.5\%$ for APs-D, 33.0 ± 14.8 and $-9.4 \pm 7.8\%$ for no

change, 54.8 ± 9.0 and $87.8 \pm 28.7\%$ for APs-P). The dotted line indicates the fit with a parabolic function ($r^2 = 0.83$, $p < 0.01$, F-test).

Except for a few experiments, in SLM-2PM recordings we did not acquire the fluorescence signals during the HFS in order to minimize the interference with GrCs activity during the induction. Nevertheless, the limited data acquired allowed to infer a correlation between the $\Delta F/F_0$ signals during the induction protocol and the percentage changes observed thereafter, as shown in Figure 4.7 (c). Also for these data the relationship between the parameters showed a U-shape curve, indicated by a dotted line (average $\Delta F/F_0$ values during HFS and average percent change after HFS: 4.7 ± 1.0 and $-63.8 \pm 6.2\%$ for CaR-D, n = 9, 9.4 and -9.9% for no change, n = 2, 10.3 and 82.85% for CaR-P, n = 2; $r^2 = 0.56$, not significant).

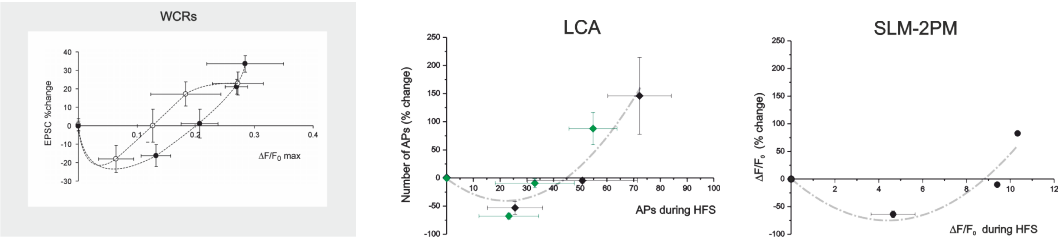

(a) (b) (c)

Figure 4.7: *Both LCA and SLM-2PM experiments reveal bidirectional plasticity.* In (a) the relationships between intracellular calcium changes, $[Ca^{2+}]_i$, and synaptic plasticity obtained through WCRs, using different stimulation frequency (•) and different durations (∘) are shown (reported from [5]). In (b) and (c) results from LCA and SLM-2PM measurements are shown, respectively. In particular, (b) shows the relationship between the number of GrCs APs emitted during the HFS and the percent change observed after the induction protocol, both for unstained (⧫) and for stained (⧫) slices; in (c) the relationship between the $\Delta F/F_0$ signals acquired during the HFS and the percent change observed thereafter is reported. The dashed line drawn through the points of each data set indicates the BCM-like and the U-shape relationships observed between the parameters.

4.4 Comparison with local field potential measurements

We compared data obtained with SLM-2PM and LCA measurements with previous multi-electrode array (MEA) experiments. These latter recorded the extracellular field potentials evoked by mfs electrical stimulation, that in the cerebellar granular layer result in a N_1-N_2-P_2 complex. In particular, N_2 is determined by granular layer postsynaptic activity and, at high stimulus intensity, it splits into multiple components, the first two of them named N_{2a} and N_{2b} (as shown in Figure 4.8 (a), [8]). Since MEA long-term plasticity experiments revealed both LTP and LTD, it was investigated whether there was a correlation between plasticity and the N_{2a} control peak amplitude, both in control condition and with inhibition blocked (obtained by adding 10 μM bicuculline in the extracellular solution). As reported in Figure 4.8 (b), plasticity showed a biphasic behavior respect to the N_{2a} control values, with LTD at low initial N_{2a} peak amplitude, LTP at high N_{2a} amplitude and a switch between LTD and LTP at intermediate N_{2a} amplitude levels. Furthermore, some data points (enclosed by a dotted circle) showed LTP in the very low N_{2a} amplitude region, possibly corresponding to synapses with low initial release probability [7, 8].
We investigated whether a similar relationship could be observed both for SLM-2PM and LCA data. Thus, we correlated the percent changes observed after plasticity induction with the stimulus-induced average control values of (i) the $\Delta F/F_0$ peak amplitude, for two-photon calcium imaging data, and of (ii) the number of APs, for LCA data. Results are shown in the upper panels of Figure 4.9 (a) and (b), respectively. Both graphs show a similar trend with predominant potentiation incidence for very low control values of the parameters (the $\Delta F/F_0$ peak amplitude and the number of spikes) and depression for low initial values (a dotted line, obtained by interpolating the data with the same function used in [8], highlights these trends in both graphs).

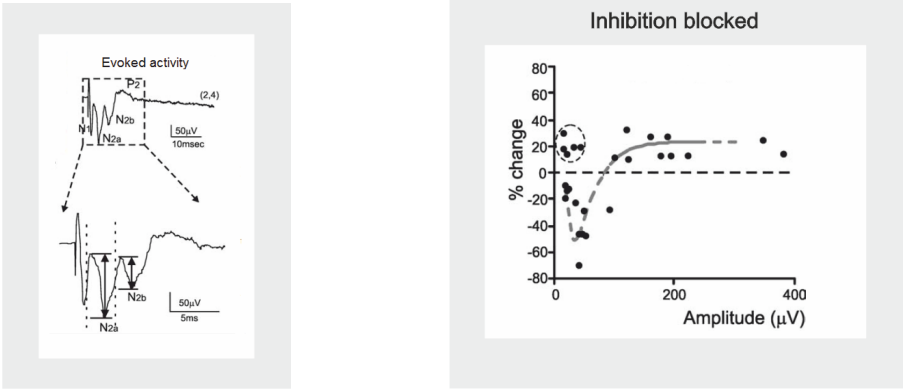

(a) (b)

Figure 4.8: *MEA recordings from the cerebellar granular layer.* In (a) an example of granular layer field potentials evoked by mfs stimulation is reported; the N_1-N_2-P_2 complex is shown, while the inset shows an enlarged view of the response, with vertical arrows indicating the amplitude of N_{2a} and N_{2b}. In (b) the relationship between plasticity and excitation measured as N_{2a} control amplitude is shown. Note that some data points in the very low amplitude region showed LTP (enclosed in a dashed circle). The data were interpolated with a double exponential equation [$y = y_0 + A_1 \cdot \exp(-(x\text{-}x_0)/\tau_1) + A_2 \cdot \exp(-(x\text{-}x_0)/\tau_2)$]. Both adapted from [8].

These relationships are in agreement with the initial phase of the trend reported in Figure 4.8 (b), which corresponds to low values (< 150 μV) of the N_{2a} control peak amplitude. On the other hand, the switch to potentiation for high initial values of the parameters (the $\Delta F/F_0$ peak amplitude and the number of APs) is not so clear as in MEA experiments, especially in SLM-2PM data, as shown in the insets of Figure 4.9 (a) and (b), respectively, which are expanded sections of the upper traces. As further discussed below, this is likely related to a different cellular sampling.

MEA recordings allowed to reconstruct the spatial organization of synaptic plasticity in the granular layer, by performing experiments both in control solution and with the addition of a GABA-A receptor blocker in the extracellular solution (10 μM bicuculline) [8]. The spatial profiles of plasticity obtained in these two conditions resemble one each other, with a LTP core surrounded by LTD; nevertheless in control

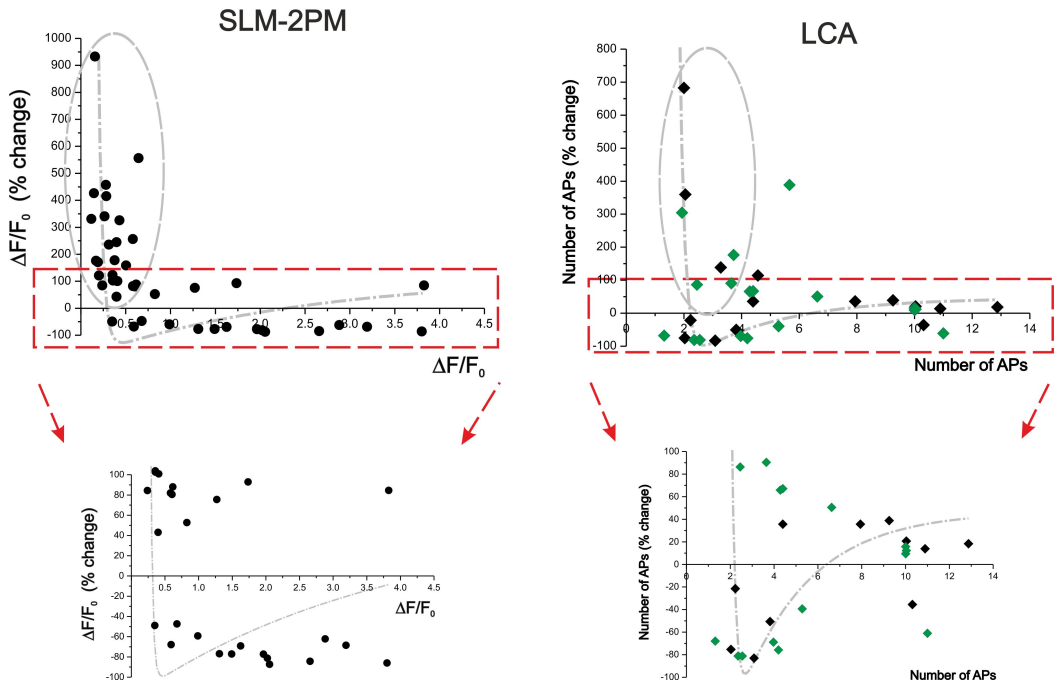

(a) (b)

Figure 4.9: *SLM-2PM and LCA recordings reveal a relationship between plasticity and excitation similar to the one observed in MEA experiments.* The relationship between plasticity and excitation was investigated both in SLM-2PM and in LCA measurements. The resulting plots are shown in (a) and (b), respectively (only data showing significant changes after HFS were reported). In particular, the excitation was measured as $\Delta F/F_0$ control values in (a), and as control number of APs in (b). In this latter, data from LCA experiments on unstained (♦) and stained slices (♦) are shown together. In order to highlight the trends similar to the previous one (see Figure 4.8 (b)), the same equation reported in [8] was used to interpolate both the data sets (dotted lines, not significant), while dashed circles indicate data points in the very low control values region showing CaR-P and APs-P, respectively. In the bottom insets, expanded sections of the regions enclosed in red squares in the upper figures are shown.

condition (data not shown) both the LTP and the LTD regions appeared more pronounced than when inhibition was blocked. In this latter condition, indeed, the magnitude of both LTP and LTD decreased respect to the control condition, and their spatial distribution was less clearly defined, as shown in Figure 4.10 (a).
In the SLM-2PM experiments described in the previous paragraphs, in order to generate minimal disturbances to cellular processes involved in plasticity expression, the illumination patter was maintained at lower intensity than in previous investigations [1, 2], thereby reducing the number of GrCs that could be reliably measured in each experiment. Nevertheless, collected data allowed us to generate a preliminary plasticity map. The spatial distribution of plasticity revealed in SLM-2PM experiments performed with synaptic inhibition blocked (i.e. gabazine perfusion) was similar to that shown in Figure 4.10 (a). The average SLM-2PM plasticity map was generated by centering the normalized plasticity maps of different experiments (n = 3) on their maximal CaR-P and aligning the slices along the mf bundle. Figure 4.10 (b) shows this resulting map: a CaR-P core emerges surrounded by CaR-D regions. As mentioned above, this is a preliminary result, thus it can only give qualitative information.

4.5 CaR-P and CaR-D in IB2 mice

Recent evidences suggest that the cerebellum is implicated in autism spectrum disorders (ASDs), as well as in other several neurological disorders [45, 46]. To investigate cerebellar alterations, different animal models have been developed. Among these, the IB2 KO mouse model has been extensively studied in our lab [47]. The IB2 KO mice are mutant mice characterized by an altered glutamatergic transmission in the cerebellum resulting in a 3.3-fold increase in the NMDA/AMPA ratio at the mf-GrCs synapses [47]. Given the key role of NMDA receptor (NMDA-R) activation in long-term plasticity induction at the mf-GrCs relay [5, 6, 7] and the assessed glutamatergic origin of SLM-2PM calcium signals, we performed preliminary SLM-2PM long-term plasticity experiments on IB2 KO cerebellar slices to further investigate

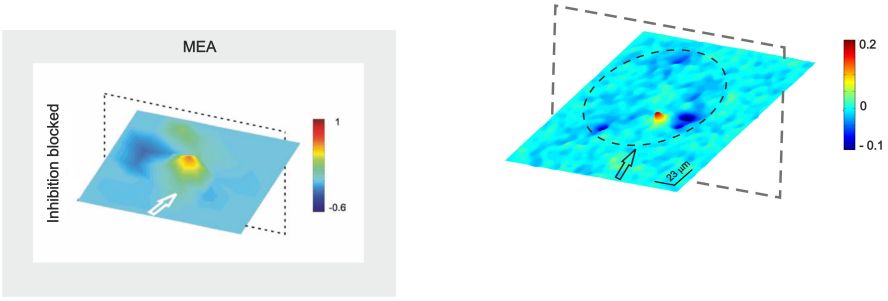

(a) (b)

Figure 4.10: *The spatial organization of synaptic plasticity in condition of blockage of inhibition.* (a) Plasticity map obtained with MEA recordings performed with inhibition blocked, reported from [8]. (b) SLM-2PM long-term plasticity experiments performed in the same condition revealed a spatial profile of plasticity similar to that reported in (a). In both the maps the arrows indicate the mf bundle direction, while in (b) the region from which the fluorescence signals were acquired is indicated with a dashed circle.

the cerebellar microcircuit dysfunctions in these mice.

Similarly to what observed in long-term plasticity experiments performed on rat and IB2 WT mouse slices (extensively reported in section 4.1), IB2 KO GrC calcium signals showed persistent variations after the plasticity induction, both as CaR-P and as CaR-D (CaR-P: $+309 \pm 24.3\%$, n=13, 30 min after HFS; CaR-D: $-57.5 \pm 2.7\%$, n=18, 30 min after HFS, $p < 0.005$ for both, for WT mice; CaR-P: +301%, n=2, 30 min after HFS; CaR-D: $-57.5 \pm 2.7\%$, n=9, 30 min after HFS, $p < 0.005$, for KO mice).

Fiigure 4.11 (a) and (b) shows results from IB2 WT (●) and KO (●) GrCs together, for the different post HFS trends (CaR-P and CaR-D, respectively). No significant differences were found between IB2 WT and KO GrCs showing CaR-D ($p = 0.53$), while an impressive increase in the first phase of CaR-P can be observed in KO mice respect to their WT littermates ($+225.9 \pm 25.5\%$, n=13, 22 min after HFS, for WT mice and $+489.6 \pm 81.4\%$, n=2, 22 min after HFS, for KO mice). Nevertheless, given the low number of KO GrCs showing CaR-P it was not possible to perform a statistical analysis.

In Figure 4.1 (c) and (d) the incidence histograms of CaR-P, CaR-D and no change are shown for IB2 WT and KO GrCs, respectively (CaR-P: 36.11%, CaR-D: 50%, no change: 13.89% for IB2 WT GrCs and CaR-P: 18.18%, CaR-D: 81.81% for IB2 KO GrCs).

These preliminary results are in agreement with other observations from our lab. In particular, in WCRs, after the induction protocol, a significant increase in EPSC amplitude was observed in IB2 KO GrCs as compared to WT GrCs ($120.6 \pm 49.3\%$ vs $35.6 \pm 10.6\%$ respectively, $n = 12$ for KO and $n = 13$ for WT, $p < 0.05$, (Soda *et al.*, *manuscript in preparation*)). In order to compare the SLM-2PM and the WCRs results, in Figure 4.11 (e) and (f) we show the histograms of the percent change values observed after induction for both the SLM-2PM experiments and the WCRs, respectively.

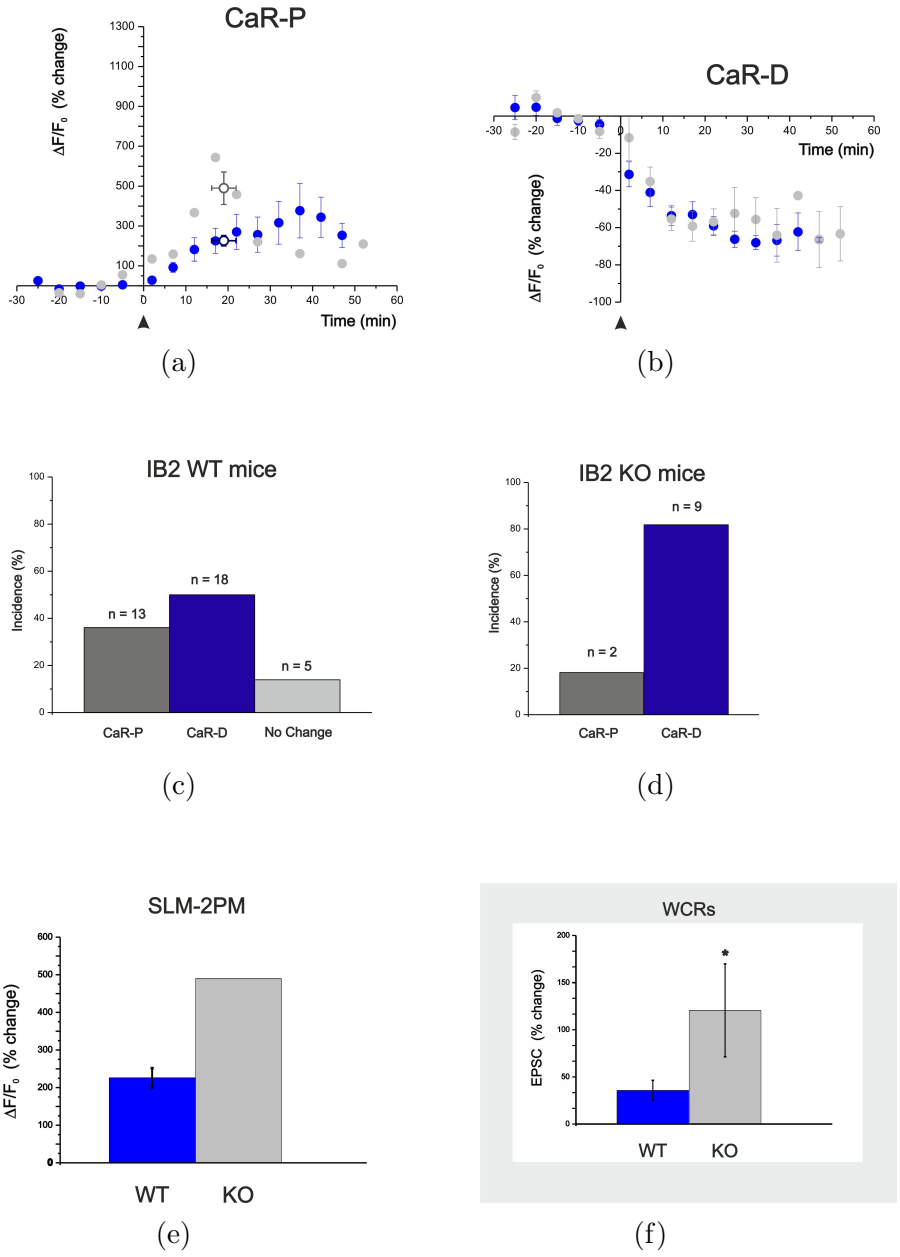

Figure 4.11: *The SLM-2PM reveals calcium-related long-term plasticity in IB2 KO mice.* A HFS plasticity protocol delivered to the mfs bundle induced persistent variations in calcium signals amplitude from IB2 WT (●) and KO (●) GrCs, both as CaR-P (a) and as CaR-D (b). The impressive increase observed in the first phase of KO CaR-P respect to WT is highlighted in (a) by indicating the average values of CaR-P observed 22 minutes after the induction (○ and ○ average values for WT and KO GrCs, respectively). Both in (a) and in (b) the HFS is indicated by an arrowhead and data points are reported as mean ± s.e.m..
In (c) and (d) incidence histograms of Car-P and CaR-D for WT and KO mice are shown, respectively, while histograms in (e) and (f) show the average value in the amplitude of CaR-P and LTP percent changes observed through SLM-2PM experiments and WCRs (reported from Soda *et al.*, *manuscript in preparation*), respectively.

4.6 Comparison between experiments and models[1]

A realistic large-scale network model of the cerebellar granular layer was developed in our lab through a "bottom-up" approach in which the system is reconstructed through a reverse engineering process on the basis of available anatomical and functional informations. With this approach, the functional properties of the network emerge from the properties of constitutive elements and from their synaptic organization [24, 48, 49, 50, 51, 52, 53, 54, 55]. The model was written in NEURON-Python and was used to simulate a network with a size sufficient to reproduce a functionally relevant portion of the cerebellar granular layer, in which the connectivity representation was elaborated respecting experimentally derived ratios and geometries. In particular, GoCs were excited through mossy and parallel fibers, coupled through gap junctions, and inhibited by reciprocal inhibitory synapses. By reconstructing the granular layer from elementary properties and relevant biological data on single neurons, the model needs to be validated against experimental data that have not been used for reconstructions. To this aim, previous SLM-2PM results were elaborated and used to confirm modeling ones.

As described in paragraph 3.5, the SLM-2PM data allowed to reconstruct the spatial organization of activity in the granular layer, which resulted characterized by a center-surround structure, with strong excitation in the core and inhibition in the surround, as shown in Figure 4.12 (a). In order to assess if network model was able to reproduce this characteristic, the granular layer activity was simulate in a 220x200 μm^2 granular layer network, both in control condition and in condition mimicking the blockage of inhibition. The network activity was elicited by stimulating 10 *glomeruli* with the same stimulation protocol used in the SLM-2PM experiments (10 pulses at 50 Hz), while the condition of blockage of inhibition was simulated by turning off both the GoCs tonic activity and the activity of GoCs contacted by the stimulated *glomeruli*. Results obtained in these simulations allowed to reconstruct an excitatory/inhibitory

[1]The results of the network modeling were kindly granted by Dr Stefano Casali.

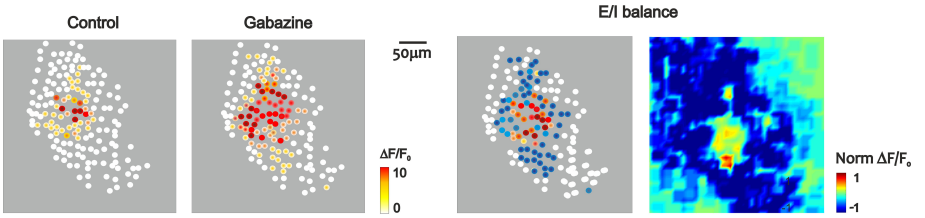

(a)

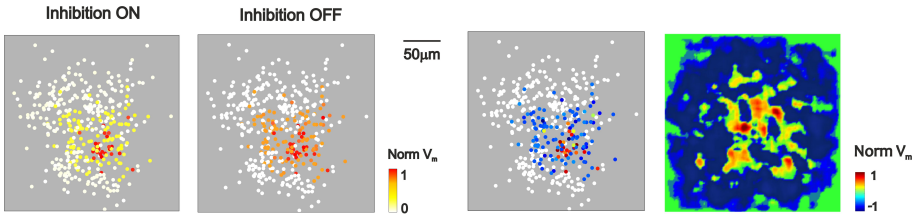

(b)

Figure 4.12: *SLM-2PM results validate modeling data.* The granular layer model reproduced the properties of the granular layer activity experimentally observed, such as the effect of blockage of inhibition on the spatial distribution of GrC activity and the resulting characteristic center-surround profile. Results from SLM-2PM experiments and from the network model are shown in (a) and (b), respectively. Note the remarkable similarity between maps obtained from real data and from model ones.

(E/I) balance map similar to the one obtained through the SLM-2PM data, as shown in Figure 4.12 (b).

Thus, the network model is able to remarkably reproduce the properties of granular layer activity observed with SLM-2PM experiments, including the effect of blockage of inhibition on the spatial distribution of GrCs activity and the emergence of a center-surround profile describing the balance between excitation and inhibition.

4.7 Results summary

In this chapter we reported the data obtained with SLM-2PM and LCA recordings and the comparisons made between these and previous results.
Herein, these results are briefly summarized:

- we performed long-term plasticity calcium imaging experiments with the SLM-2PM from multiple GrCs simultaneously. After the plasticity induction, we observed persistent calcium signal variations, both as CaR-P and as CaR-D;

- CaR-P showed impressive variations in signal amplitude. We investigated the nature of these changes by comparing SLM-2PM results with those from previous WCRs showing that GrCs intrinsic excitability increases after the induction of plasticity. Since SLM-2PM $\Delta F/F_0$ signals are linearly correlated to the number of GrCs spikes, we inferred that the percent changes observed in CaR-P could be explained as a combination of changes in GrCs intrinsic excitability and in synaptic transmission;

- we performed patch-clamp experiments in LCA configuration in order to highlight the neuronal activity variations underlying CaR-P and CaR-D. Also in these experiments, we observed a potentiation and a depression of the number of the stimulus-induced GrCs APs after plasticity induction, with percent change values and incidences similar to those observed in SLM-2PM calcium imaging experiments;

- GrC electroresponsiveness observed through LCA experiments resulted comparable with those from previous WCRs. APs-P magnitude negatively correlated with the probability of AP generation in response to a single stimulus (which in turn is linked to the probability of quantum release on the presynaptic terminal);

- we observed a U-shape relationship between the GrCs activity during the HFS protocol (both as $\Delta F/F_0$ signals and as number of APs emitted) and the GrCs trends after plasticity induction, in agreement with previous ones noted with WCRs;

- CaR-P and CaR-D from SLM-2PM experiments as well as APs-P and APs-D from LCA experiments showed a dependency on the pre-plasticity state similar to that observed with MEA measurements; SLM-2PM experiments revealed a spatial organization of plasticity similar to that observed through MEA recordings;

- we performed preliminary SLM-2PM plasticity experiments on IB2 WT and KO mice to investigate neurotransmission alterations in the KO mice granular layer. We observed CaR-P as well as CaR-D both from WT and KO GrCs; moreover, CaR-P showed an impressive increase in KO GrC as respect to WT, in agreement with EPSC percentage variations observed in WCRs;

- we further elaborated the previous SLM-2PM results to validate the granular layer network model developed in our lab.

Part III

Discussion

The SLM-2PM technology was developed in our lab basing on previous articles showing that (i) two-photon illumination can be used to excite fluorescence and that (ii) arbitrary illumination patterns can be generated through spatial light modulators [15, 56, 57].

Previous calcium imaging experiments performed through the SLM-2PM allowed to study the spatio-temporal organization of the cerebellar cortex [1, 2]. These results validated the SLM-2PM as an effective technique able to investigate multiple cells activity, simultaneously. Furthermore, through these experiments the synaptic origin of fluorescence calcium signals was proved as due to glutamate receptors activation, and the relationship between these signals and the neuronal electroresponsiveness was assessed, as briefly reported in Chapter 3. However, it was unclear whether the SLM-2PM could be used to investigate other properties of the neuronal activity, such as long-term plasticity.

In this work, we demonstrated that the system can be used to study neuronal plasticity. SLM-2PM long-term plasticity calcium imaging experiments performed on rat and mouse cerebellar slices, indeed, revealed persistent changes in GrCs calcium signals. To investigate the underlying mechanisms, we performed LCA patch-clamp experiments. Finally, we compared SLM-2PM as well as LCA results with pre-existing data from WC and MEA recordings.

In the following sections these results will be thoroughly discussed.

SLM-2PM revealed long-term plasticity through persistent calcium signals variations In this study long-term plasticity at the mf-GrC synapses was investigated through the SLM-2PM technology. To this aim, stimulus-induced calcium signals from rat and mouse GrCs somata were acquired before and after a HFS protocol delivered to the mfs bundle to induce long-term plasticity.

As proven in [4, 5, 8, 31], mf-GrC synapses express bidirectional long-term plasticity depending on (i) the pre-induction GrC state and on (ii) GrC $[Ca^{2+}]_i$ during mfs input bursts. During the plasticity induction the main contribution to the changes in $[Ca^{2+}]_i$ in GrCs is given by NMDA-Rs activation. The Ca^{2+} influx can be then reinforced by the activation of metabotropic glutamate receptors (mGlu-Rs), voltage-dependent calcium channels (VDCCs) [58] and Ca^{2+}-induced Ca^{2+}-release (CICR) mechanisms, resulting in a signal amplification [59, 60]. As shown in [6, 61, 62], the NMDA-Rs and mGlu-Rs coactivation is needed for plasticity induction; although the activation of these receptors is confined to GrC dendrites, due to the GrC high electrotonic compactness [63, 64, 65], the consequent membrane depolarization will be homogeneously distributed. Thus, whether a mf-GrC synapse develops long-term potentiation or depression will depend on local glutamate receptor activation and on global membrane potential control [4].

In SLM-2PM experiments, we observed persistent changes of calcium signals amplitudes after the induction protocol, both as long-term potentiation (CaR-P) and as long-term depression (CaR-D), while some GrCs showed no changes in signal amplitudes. In the initial post-induction phase, CaR-P and CaR-D time courses showed percent changes comparable to those observed in EPSC measurements [5, 7]; however, SLM-2PM signals amplitudes further increase (or decrease, respectively) until thirty minutes post induction, when they reached stable values ($+388 \pm 34.3\%$ and $-73.8 \pm 2.5\%$, respectively). All the Ca^{2+} sources described above likely concur to generate the CaR-P increase (or CaR-D decrease, respectively) observed but we may speculate that an increase (or decrease) in the sensibility of Ca^{2+} signaling toolkit (e.g. an increase of the IP_3 receptors sensitivity) could also be involved [66, 67, 68, 69]. As reported in [3], after plasticity induction there is a three-fold increase of the probability of firing in GrCs. Basing on the linear correlation between fluorescence

signals and GrC spikes, we computed the $\Delta F/F_0$ changes related to a three-fold increase in the number of emitted spikes. These values resulted comparable to those observed in CaR-P, suggesting that GrCs intrinsic plasticity could contributed to CaR-P. Furthermore, since the SLM-2PM calcium signals were acquired from GrC somata, and considering the role of Ca^{2+} in regulating the late-phase LTP, it can not be ruled out that the high percent changes observed at the end of the CaR-P time course can indicate an initial expression of late-phase LTP. Nevertheless, a detailed study of Ca^{2+} sources and mechanisms involved in SLM-2PM calcium signals was beyond the purpose of this work and it was not conducted.

In D'Errico *et al.* high EPSC percent changes (+100.6± 42.8%) were observed after HFS in recordings performed at 34°C. However, other previous WCRs conducted at 30°C (the same temperature maintained during SLM-2PM experiments) did not evidenced high value of EPSC changes (average percent change around 30%, [6, 7]). Therefore, even if a minor contribution of the recordings temperature to the percentage values reached in CaR-P could be present, we can rule out a close relationship between them.

In most of the experiments, a major incidence of potentiation over depression and no change was observed, in accordance with the condition of blockage of inhibition maintained during the recordings (i.e. GABA-A receptors blocker perfusion). Nevertheless, in measurements performed on mouse slices, CaR-D seems to prevail over CaR-P. The CaR-P and CaR-D ratio strongly depend on uncontrolled conditions as the number of mfs recruited by the stimulation and the ratio between the activation or the failure of activation of all the synapses impinging on a given GrC. Moreover, since GrCs from both rat and mouse slices were recorded from the same cerebellar lobules (i.e. the central lobules), it is unlikely that the differences observed between incidence ratios in rat and mouse recordings have any physiological significance.

LCA experiments confirmed SLM-2PM observations LCA experiments were performed to unravel the neuronal activity changes underlying CaR-P and CaR-D. Stimulus-induced APs were acquired before and after the plasticity induction, both on

unstained and on Fura-2 AM stained rat cerebellar slices. Also in these experiments the trends noted in SLM-2PM measurements were observed, with average percent changes and time courses similar to the ones related to calcium signals. Moreover, a major incidence of APs-P over APs-D and no change was observed, both for unstained and for stained slices, again reflecting the condition of blockage of inhibition maintained during the experiments.
In experiments showing APs-P, a variability in the percent changes reached can be observed between unstained and stained slices and between these average values and the average CaR-P ones. Rather than due to a physiological difference, this variability is likely related to a different sampling between LCA and SLM-2PM experiments, both as different number of GrCs recorded and as different pre-induction GrCs states (see the following discussion).
The APs-P, APs-D and no change behaviors observed in unstained and in stained slices were compared and no significant differences were found between them. As the same behaviors were observed with the SLM-2PM, this corroborates the assumption that the extrinsic Ca^{2+} dye used in calcium imaging experiments did not interfere with efficient Ca^{2+} homeostasis and neuronal functional properties [65]. Thus, the SLM-2PM can be employed also to study phenomenons involving sensitive intracellular processes.

The relationship between plasticity and the pre-induction GrC state We investigated whether we could find a relationship between plasticity and (i) the $\Delta F/F_0$ calcium signals (for SLM-2PM recordings) and (ii) the number of APs (for LCA experiments) recorded during the HFS protocol. In both cases, a U-shape relationship was assessed, with depression expressed both for low values of $\Delta F/F_0$ calcium signals and for low number of APs observed during the induction and, after a neutral point, potentiation at relatively high values of $\Delta F/F_0$ calcium signals and high number of APs observed during the HFS protocol. These relationships resemble previous ones shown in [4] and in [5]; nevertheless, in these latter the differences in $[Ca^{2+}]_i$ during the induction were due to the different plasticity protocols used, while both in SLM-2PM and in LCA experiments the same induction protocol was applied.

Thus, in SLM-2PM and LCA recordings the different values in $[Ca^{2+}]_i$ and in the number of emitted APs are likely related to the GrCs state during the HFS, which, in turn, is related to the GrC pre-induction state. This hypothesis is supported by the relationships observed both in SLM-2PM and in LCA data by correlating the percent changes observed after plasticity induction with the average control values of both the $\Delta F/F_0$ peak amplitude and the number of APs. These trends are similar to that depicted in [8] which shows that, also in condition of blockage of inhibition, if excitation does not pass the threshold for LTP induction (due to a low absolute depolarization or to a high initial probability of release), LTD can be expressed. This hypothesis was indeed demonstrated in other previous articles, [6] and [3], in which the plasticity protocol was paired with GrCs' membrane hyperpolarization: by preventing the Mg^{2+} block removal from NMDA-Rs and the consequent membrane depolarization, this causes the inefficacy of the induction. Moreover, in [3] it was demonstrated that there is a correlation between the EPSP size recorded before the induction (which in turn is linked to the membrane potential value at the resting state) and the efficiency of the induction protocol, and thus the LTP magnitude reached.
Given the minor control of the SLM-2PM and LCA recordings to the neuronal state, and especially the lack of membrane potential control during the plasticity induction, it is not surprising that potentiation, depression and no changes were observed in both SLM-2PM and LCA experiments.

Calcium-Related plasticity in IB2 mice Preliminary long-term plasticity SLM-2PM experiments were performed on IB2 WT and KO mice (a recent animal model of ASDs), in order to investigate neurotransmission alterations in the granular layer. Also in these measurements, calcium signals amplitudes showed changes after the induction protocol persisting until the end of the recordings, both as CaR-P and as CaR-D. Their temporal trends were similar to those observed in recordings from rat slices, with a continuous increase (decrease, respectively) in signal amplitudes until about thirty minutes after the induction protocol. Moreover, although the data

set is limited, there is an apparent excess of CaR-P in KO over WT mice, which is most apparent in the first twenty minutes after the induction. Around this time, indeed, KO CaR-P is about three times bigger than in WT. While these data need to be extended, they are in line with WCRs performed in our laboratory (Soda *et al., unpublished results*).
As in experiments performed on rat cerebellar slices, also during these measurements the GABA-A receptors blocker gabazine was perfused. Nevertheless, a major incidence of CaR-D over CaR-P was observed. As discussed above, this is likely due to different uncontrolled conditions during the experiments, such as the number of mfs recruited by the stimulation, unlike that due to different physiological conditions. Furthermore, when comparing data from WT and KO GrCs, we can observe a low number of GrCs showing CaR-P in KO mice than in WT. Since no significant differences were found between these two data sets, this is likely related to the current low data sampling.

Comparison between SLM-2PM and modeling results Computational models are critical to interpret the complex patterns of activity of neurons and neural networks and to explain how these patterns originate from the wealth of mechanisms characterizing the underlying biological systems. Nevertheless, in the "realistic modeling" strategy they need to be validated against experimental data that have not been used for reconstructions. SLM-2PM results, by describing the spatial organization of the granular layer with the single-cell resolution, were well adapted for this need. The remarkable similarity that could be observed between real and model data allowed to validate the network model developed in our lab. SLM-2PM long-term plasticity experiments results will be further used to validate future model data describing plasticity in the granular layer.

In conclusion, the SLM-2PM recordings proved for the first time that long-term plasticity at the mf-GrCs relay can be observed also as persistent variations of $[Ca^{2+}]_i$ recorded from GrCs' somata.
In SLM-2PM and LCA experiments, both long-term potentiation and depression

of signals were observed, thus confirming the existence of LTP and LTD at the mf-GrC synapses and proving the assumptions and the results reported in previous electrophysiological articles [4, 5, 8]. As discussed above, the GrCs activity during the plasticity induction was relevant in determining the sign of plasticity; this activity, in turn, is linked to the GrCs initial responsiveness which thus results to be the most critical factor in defining the sign of plasticity.

As demonstrated in [3, 6, 7, 49], long-term plasticity at the mf-GrC synapses is related to changes in both pre- and post- synaptic mechanisms. Thus, the persistent variations observed both in SLM-2PM and in LCA experiments most likely reflect a combination of synaptic and non synaptic plasticity.

Since from previous results ([1, 2]) it was unclear whether the SLM-2PM could be used to investigate long-term changes of neuronal activity, the most of this work is focused on the validation of the SLM-2PM technology for these kind of experiments. To this aim, at the moment, in order to generate minimal disturbances to cellular processes involved in plasticity expression, the illumination patter was maintained at lower intensity than in previous investigations [1, 2], thereby reducing the number of GrCs that could be reliably measured.

As previous works proved that bidirectional mf-GrC plasticity is critical for network reconfiguration and for the optimization of transfer information [4, 26, 70], the SLM-2PM will allow to obtain a further improvement in the understanding of the way in which the cerebellar granular layer processes incoming patterns.

Future developments

In this study we validated the SLM-2PM as an effective technique that can be used to investigate long-term plasticity in multiple cells simultaneously. The single-cell resolution achieved with the system will enable the study of neuronal microcircuits activity and its temporal changes in consequence of different inputs.
To this aim, a variety of experiments could be performed through the SLM-2PM. Concerning the long-term plasticity recordings, the compromise between the intensity of the illumination pattern and the number of cells monitored per experiment will be improved, in order to reconstruct the activity pattern of large populations of neurons before and after the induction of plasticity.
The cerebellar local microcircuit will be investigated by acquiring calcium signals from different cerebellar cortex neurons simultaneously also in control condition (i.e. without the blockage of inhibition). The spatio-temporal organization of granular layer plasticity will be investigated using specific input patterns and recording signals from numerous GrCs and GoCs in order to assess a main theory predicting that plasticity is first stored in an oscillating GoCs interneuron network and then transferred to GrCs through STDP mechanisms.
Pharmacological experiments could be performed to unravel the molecular mechanisms underlying the biphasic temporal trends observed both in CaR-P and CaR-D.
In recent works, the SLMs were incorporated into traditional two-photon microscopes to image neuronal activity in three dimensions [16, 71, 72]. As shown in [2], also through the SLM-2PM it is possible to acquire 3D images of cells. Thus, a further software development could be achieved to acquire simultaneous multi-plane signals

and to perform *in vivo* experiments.

Part IV

Appendix

Fluorescence

Fluorescence is a physical phenomenon in which a molecule (i.e. fluorophore) absorbs electromagnetic radiation at a specific wavelength and nearly immediately (within $\sim 10^{-8}$ s) emits radiation (i.e. fluorescence light) at a different wavelength. Figure 13 depicts an example of Jablonsky diagram, commonly used to illustrate the process. Both the absorption and the emission processes can take place between different vibrational levels of the involved energy states of the molecule (S_0 ground energy state, S_1 excited energy state).

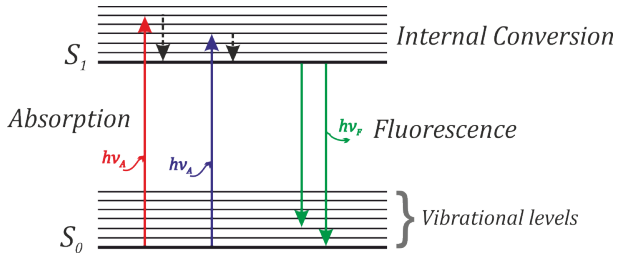

Figure 13: *Example of a Jablonski diagram.* The figure shows the electronic states of a molecule and some possible transitions between them.

In most cases, before the emission, internal conversion transitions bring the excited molecule to the lower vibrational level of S_1. As a consequence, the energy gap for the emission process is usually lower than that for the excitation, and the photon will be emitted with a longer wavelength than that absorbed (Stokes shift). Another

consequence of internal conversion processes is that the emission spectrum observed is generally the same, irrespective of the excitation wavelength (Kasha-Vavilov rule) [73].

Two-photon excitation fluorescence Traditionally, the transition from S_0 to S_1 is reached through the absorption of one photon. The same result can be obtained by the near-simultaneous (within $\sim 10^{-16}$ s) absorption of two-photons; in this case, the fluorophore is excited to a "virtual" intermediate state through the absorption of one photon, while a second photon further excites it to S_1, as shown in Figure 14. The two-photons have approximately half the energy (thus double the wavelength) of the photon required for a single photon excitation event to occur [74, 75].

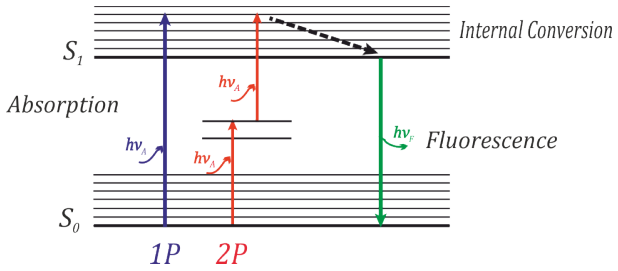

Figure 14: *Comparison between one- and two-photon excitation.* In one-photon excitation a single photon is required for the transition from S_0 to S_1; in two-photon excitation the same transition occurs through the absorption of two photons having half the energy compared to the single photon.

Two-photon excitation is a nonlinear process in which the absorption rate depends on the square of the light intensity. The probability that this event occurs is extremely low. Thus, an adequate photon flux with both temporal and spatial concentration is needed. The first requirement is achieved using mode-locked femtosecond pulsed lasers as light source, such as Titanium:Sapphire crystal-based lasers. These use a titanium-doped sapphire crystal as gain medium, allowing wavelength tunability from ∼700 to ∼1000 nm, while the high intensity photons pulses required are produced

in a periodic sequence through a Kerr lens mode-locking process allowing to obtain extremely brief ($\sim 10^{-13}$ s) pulses with a high repetition rate (80-100 MHz). The spatial focusing can be achieved through a high numerical aperture objective. In this way, indeed, the photons are sufficiently numerous to interact simultaneously with a fluorophore and to generate an appreciable amount of two-photon excitation only at the focal point.
The light intensity drops off quadratically with distance above and below the focal point, so excitation outside the focal point does not occur and fluorophores are excited almost exclusively in an ellipsoid femtoliter volume, as shown in Figure 15 [76, 77].

Figure 15: *Spatial confinement of two-photon fluorescence emission.* Fluorescence emission obtained with one-photon (double cone, above) and two-photon (bright dot, pointed by the arrow, below) excitation. The spatial confinement reached through two-photon excitation is extremely clear; out-of-focus contributions are absent. Reported from [78].

Two-photon excitation microscopy Two-photon excitation microscopy is an imaging technique that has evolved as a suitable alternative to conventional one-photon microscopy; its application to fluorescence microscopy has become a powerful tool for studying biological structure and activity *in vitro* and *in vivo*.

The main advantages over one photon excitation microscopy derive from two-photon excitation characteristics described in the previous paragraph. Since the excitation is localized, the three-dimensional contrast and resolution are achieved without the need of spatial filters in the detection path (i.e. pinholes in the confocal microscope). Moreover, the longer wavelengths used for two-photon excitation penetrate the tissue better than visible wavelengths used in one-photon excitation, resulting in deeper penetration of the focused laser beam. Finally, photobleaching and photodamage are eventually localized only to the focal plane and multiple fluorophores can be excited simultaneously [75, 76, 77].

Fluorophores Regardless of the way in which the transition occurs, the features of the fluorescence emission are related to the fluorophore used. These can be intrinsic (i.e. naturally occuring) or extrinsic molecules (i.e. fluorescent molecules added to the sample). These latter can be used to obtain images of different structures of a cell or they can bind to ions as activity or concentration indicators, in order to measure biochemical functions [78, 79]. Each fluorophore has its own characteristics, described through a set of parameters which have to be considered when choosing which one to use. Some of these are: the excitation and emission spectra, the quantum yield (i.e. the ratio of the number of emitted photons to that of absorbed photons), the absorption cross section (that quantifies the probability with which a particles interaction occur) and the extinction coefficient (that defines how strongly a substance absorbs light at a given wavelength) [80].

The cerebellum

Cerebellar anatomy The cerebellum is a strategic part of the central nervous system involved mainly in motor learning, movement execution as well as motor planning and cognition. It has a well defined macro structure, as shown in Figure 16: two longitudinal furrows divide it into a central area (i.e. the vermis) and two lateral hemispheres, while two deep transversal fissures subdivide it in anterior, posterior and flocculonodular lobes. Shallow fissures further divide cerebellar lobes into several lobules consisting of thin parallel folia.
The cerebellum is connected to the brain stem bilaterally by three peduncles - superior, middle and inferior- that carry information to and from it: the superior peduncle is mostly efferent, projecting fibers to the cerebral hemispheres (thalamus), midbrain (red nucleus) and pons (vestibular nuclei, oculomotor, trigeminal); the middle peduncle contains exclusively afferent fibers from the controlateral pontine nuclei; and finally, the inferior peduncle contains both afferent fibers (from the brain stem and the spinal cord) as well as efferent fibers directed to the vestibular nuclei.

Cerebellar cortex The cerebellar cortex is a continuous, largely homogeneous sheet of cells organized in three well distinguishable layers of gray matter (from the innermost to the outermost: the granular cell layer (GL), the Purkinje cell (PC) layer and the molecular layer (ML)) that enclose a deep white matter core, i.e. the *arbor vitae*, characterized by a branched tree-like appearance in sagittal sections, as shown in Figure 16 (b).
The cerebellar white matter consists mainly of myelinated afferent and efferent fibers,

as well as a cluster of gray matter, the deep cerebellar nuclei (DCN). The afferent fibers consist of mossy (MFs) and climbing fibers (CFs), originating from pontine and vestibular nuclei and from the inferior olive (IO), respectively, while the efferent fibers consist of PCs axons. Collateral projections from MFs and CFs, as well as from PCs, are sent to DCN which in turn project to the IO and to other extracerebellar sites.
The white matter inserts the inner gray matter layer, the GL. This consists predominantly of densely packed granule cells (GrCs), the smallest neurons found in the brain. Each GrC emits an average of four thin dendrites, terminating in claw-like protrusions, and a thin unmyelinated axon that ascends into the ML. Here it bifurcates into two horizontal branches, to form parallel fibers (PFs), giving rise to a distinctive T-shape. Sparsely distributed in the layer there are three other types of interneurons, about 400 times less numerous than GrCs. Golgi cells (GoCs) are uniformly distributed in the layer; they are characterized by a wide dendritic spread that makes synapses with PFs, in the ML, and in the same GL. Here they give origin to a structure consisting of GrCs dendrites, GoCs axon terminals and afferent MFs terminals, the *glomerulus*. Other two types of cells are present with a heterogeneous distribution within the GL: the Lugaro cells (LCs) and the unipolar brush cells (UBCs). The LCs are located beneath the PC layer; they are characterized by a fusiform soma and thick horizontally oriented dendrites. The UBCs are specifically located in the vestibulo-cerebellum; they have an oval cell body usually with a single short dendrite ending in a brush-like structure.
PC layer is the second innermost layer; it is a one cell thick layer in which PCs are positioned adjacent to each other. PCs are the biggest and probably the most complex neuron of the cerebellar cortex; their dendrites show a characteristic arborization that branches profusely along the parasagittal plane into the ML, making synapses with CFs and PFs. PCs project their axons to the DCN, constituting the sole output of the cerebellar cortex.
The outermost ML is cell poor; in addition to containing PCs dendrites and their afferents, two neuronal types are find in the layer, the stellate (SC) and the basket cells (BC). BCs are located in the lower third of the layer; they project their axons along the sagittal plane toward the underneath PC layer where they surround the

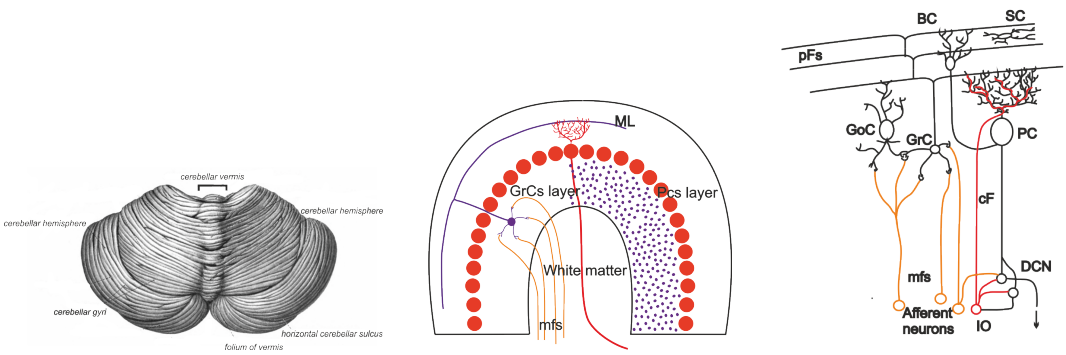

(a) (b) (c)

Figure 16: *The cerebellar anatomy.* The figure shows a posterior view of the cerebellar anatomy (a) [83], while schematic sketch of the different layers and of the different neuronal types of the cerebellar cortex are shown in (b) and (c), respectively.

PC somata with a basket-like structure. SCs are found in the outer two thirds of the ML; they are characterized by a star-like shape formed by dendritic processes radiating from the cell body and by an axonal process that expand in the sagittal plane [9, 25, 81, 82].

Calcium involvement in neuronal processes

Intracellular calcium homeostasis Calcium ions are the main second messengers in all cell types. The regulation of intracellular Ca^{2+} level (Ca^{2+} homeostasis) is an essential element for normal cellular activities. In neurons this is connected with modulation of neuronal cells processes, from neurotransmitter release to intracellular signaling transduction. In the cytosol Ca^{2+} levels ($[Ca^{2+}]_i$) are maintained at very low level (about 10^{-7} M). An increase of $[Ca^{2+}]_i$ can induce cell apoptosis and can be involved in pathological events as brain trauma, epilepsy, and other diseases. At any moment the cytosolic $[Ca^{2+}]_i$ is the result of a balance between calcium influx and efflux as well as Ca^{2+} exchange with internal stores [57]. Extracellular Ca^{2+} influx is regulated through various Ca^{2+} channels embedded within the plasma membrane (e.g voltage-dependent Ca^{2+} channels, VDCCs, or ionotropic and metabotropic glutamate receptor channels), as shown in Figure 17. Intracellular Ca^{2+} release is mediated by inositol trisphosphate receptors (IP_3R) and ryanodine receptors (RyR), while Ca^{2+} ions are removed from the cytosol by mitochondria and by the plasma membrane calcium ATPase (PMCA) as well as by the sodium-calcium exchanger (NCX); the sarco-/endoplasmic reticulum calcium ATPase (SERCA), instead, transports Ca^{2+} in the lumen of the endoplasmatic reticulum (ER) [57].
At glutamatergic synapses, such as mf-GrCs synapses, $[Ca^{2+}]_i$ changes depend on the activation of NMDA receptors (NMDA-Rs) and metabotropic glutamate receptors (mGlu-Rs) and can be reinforced by the opening of the VDCCs and by Ca^{2+} release

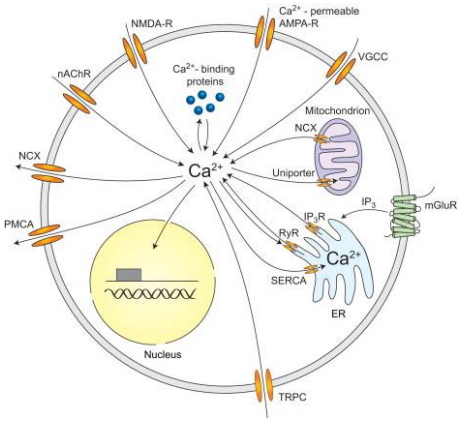

Figure 17: *Neuronal calcium signaling.* Different extra- and intra-cellular sources of Ca^{2+} influx are shown, reported from [57].

from intracellular stores [84, 85, 86].

Calcium imaging and calcium dyes Calcium imaging is an experimental technique used to show the Ca^{2+} status of a cell, as well as of a population of interconnected cells, and to study its dynamics variations. It takes advantage of fluorophores that can chelate Ca^{2+} ions and change their fluorescence properties depending on Ca^{2+} concentration values.

Two main classes of calcium indicators exist: genetically encoded calcium indicators (GECIs) and chemical indicators (i.e. calcium dyes). GECIs are encoded by DNA thus they can be delivered to the intact brain noninvasively and targeted to specific cell types or subcellular compartments [87]. Calcium dyes, instead, are extrinsic molecules having high selectivity affinity for Ca^{2+} ions. They are available in two variants: cell permeant and cell impermeant. The latter can be used for single cell staining by direct injection through a micropipette, while cell permeant dyes are used for bulk loading of cells or for *in vivo* tissue staining.

In neurons, variations in $[Ca^{2+}]_i$ can be related to neuronal activity and monitored as stimulus-induced fluorescence changes. In these measurements, recorded calcium

signals typically show a fluorescence rising phase lasting for tens of ms after the stimulation, followed by the recover of the initial fluorescence level in hundreds of ms. To study the network activity of a neuronal population, such as in acute slices, a uniform labeling of all the sample cells is required, thus a cell permeant dye is need. Fura-2 AM, by having a high fluorescence emission in Ca^{2+} free solution and a resistance to photobleaching, is suitable for bulk loading and for rapid, time-resolved measurements of cytoplasmic Ca^{2+} signals [88].

References

[1] Daniela Gandolfi, Paolo Pozzi, Marialuisa Tognolina, Giuseppe Chirico, Jonathan Mapelli, and Egidio D'Angelo. The spatiotemporal organization of cerebellar network activity resolved by two-photon imaging of multiple single neurons. *Frontiers in cellular neuroscience*, 8(92), 2014.

[2] Paolo Pozzi, Daniela Gandolfi, Marialuisa Tognolina, Giuseppe Chirico, Jonathan Mapelli, and Egidio D'Angelo. High-throughput spatial light modulation two-photon microscopy for fast functional imaging. *Neurophotonics*, 2(1):015005, 2015.

[3] S Armano, P Rossi, V Taglietti, and E D'Angelo. Long-term potentiation of intrinsic excitability at the mossy fiber-granule cell synapse of rat cerebellum. *The Journal of neuroscience*, 20(14):5208–5216, 2000.

[4] D. Gall. Intracellular Calcium Regulation by Burst Discharge Determines Bidirectional Long-Term Synaptic Plasticity at the Cerebellum Input Stage. *Journal of Neuroscience*, 25(19):4813–4822, 2005.

[5] Anna D'Errico, Francesca Prestori, and Egidio D'Angelo. Differential induction of bidirectional long-term changes in neurotransmitter release by frequency-coded patterns at the cerebellar input. *The Journal of physiology*, 587.24:5843–57, 2009.

[6] E D'Angelo, P Rossi, S Armano, and V Taglietti. Evidence for NMDA and

mGlu receptor-dependent long-term potentiation of mossy fiber-granule cell transmission in rat cerebellum. *Journal of neurophysiology*, 81(1):277–287, 1999.

[7] E Sola, F Prestori, P Rossi, V Taglietti, and E D'Angelo. Increased neurotransmitter release during long-term potentiation at mossy fibre-granule cell synapses in rat cerebellum. *J Physiol*, 557(3):843–861, 2004.

[8] Jonathan Mapelli and Egidio D'Angelo. The spatial organization of long-term synaptic plasticity at the input stage of cerebellum. *The Journal of neuroscience : the official journal of the Society for Neuroscience*, 27(6):1285–96, 2007.

[9] Jessell T.M. Kandel E.R., Schwartz J.H. *Principles of neural science*. 2000.

[10] L. De Arcangelis, H. J. Herrmann, and C. Perrone-Capano. Neuronal avalanches and brain plasticity. *AIP Conference Proceedings*, 965:237–244, 2007.

[11] A Paul Alivisatos, Miyoung Chun, George M Church, Ralph J Greenspan, Michael L Roukes, and Rafael Yuste. The Brain Activity Map Project and the Challenge of Functional Connectomics. *Neuron*, 74(6):970–974, jun 2012.

[12] John M Beggs and Dietmar Plenz. Neuronal avalanches in neocortical circuits. *The Journal of neuroscience : the official journal of the Society for Neuroscience*, 23(35):11167–77, 2003.

[13] John M Beggs. Neuronal Avalanches. *Scholarpedia*, 2(1):1344, 2007.

[14] By Rafael Yuste and George M Church. The new century of the brain. *Scientific American*, 310(3):38–45, 2014.

[15] Volodymyr Nikolenko, Brendon O Watson, Roberto Araya, Alan Woodruff, Darcy S Peterka, and Rafael Yuste. SLM Microscopy: Scanless Two-Photon Imaging and Photostimulation with Spatial Light Modulators. *Frontiers in neural circuits*, 2(December):5, 2008.

[16] Sean Quirin, Jesse Jackson, Darcy S Peterka, and Rafael Yuste. Simultaneous imaging of neural activity in three dimensions. *Frontiers in neural circuits*, 8(April):29, 2014.

[17] Adrian Cheng, J Tiago Gonçalves, Peyman Golshani, Katsushi Arisaka, and Carlos Portera-Cailliau. Simultaneous two-photon calcium imaging at different depths with spatiotemporal multiplexing. *Nature methods*, 8(2):139–42, 2011.

[18] Sheng Wang, Stephanie Szobota, Yuan Wang, Matthew Volgraf, Zhaowei Liu, Cheng Sun, Dirk Trauner, Ehud Y Isacoff, and Xiang Zhang. All optical interface for parallel, remote, and spatiotemporal control of neuronal activity. *Nano Letters*, 7(12):3859–3863, 2007.

[19] Brendon O Watson, Volodymyr Nikolenko, and Rafael Yuste. Two-photon imaging with diffractive optical elements. *Frontiers in neural circuits*, 3(July):6, 2009.

[20] P Krížek and Gm Hagen. Spatial light modulators in fluorescence microscopy. *Microscopy: Science, Technology, Applications and Education*, pages 1366–1377, 2010.

[21] Marco Dal Maschio, Francesco Difato, Riccardo Beltramo, Axel Blau, Fabio Benfenati, and Tommaso Fellin. Simultaneous two-photon imaging and photostimulation with structured light illumination. *Optics Express*, 18(18):18720–18731, 2010.

[22] Richard Courtemanche, Pascal Chabaud, and Yves Lamarre. Synchronization in primate cerebellar granule cell layer local field potentials: basic anisotropy and dynamic changes during active expectancy. *Frontiers in cellular neuroscience*, 3(July):6, 2009.

[23] Egidio D'Angelo, Paola Rossi, David Gall, Francesca Prestori, Thierry Nieus, Arianna Maffei, and Elisabetta Sola. Long-term potentiation of synaptic transmission at the mossy fiber-granule cell relay of cerebellum. *Progress in Brain Research*, 148:71–80, 2004.

[24] Egidio D'Angelo, Alberto Antonietti, Stefano Casali, Claudia Casellato, Jesus A Garrido, Niceto Rafael Luque, Lisa Mapelli, Stefano Masoli, Alessandra Pedrocchi, Francesca Prestori, Martina Francesca Rizza, and Eduardo Ros. Modeling the Cerebellar Microcircuit: New Strategies for a Long-Standing Issue. *Frontiers in cellular neuroscience*, 10(July):176, 2016.

[25] J C Eccles. The cerebellum as a computer: patterns in space and time. *The Journal of physiology*, 229:1–32, feb 1973.

[26] N. Schweighofer, K. Doya, and F. Lay. Unsupervised learning of granule cell sparse codes enhances cerebellar adaptive control. *Neuroscience*, 103(1):35–50, 2001.

[27] Masao Ito. Cerebellar circuitry as a neuronal machine. *Progress in Neurobiology*, 78(3-5):272–303, 2006.

[28] B Y David Marr. College, Cambridge. *Psicológica*, 202(617):437–470, 1969.

[29] James S Albus. A Theory of Cerebellar Function A great body o f facts has been known for many years concerning the relative simplicity o f the cerebellar cortex have fascinated anatomists since that make possible comprehensive theories o f cerebellar function . A great. *Mathematical Biosciences*, 10:25–61, 1971.

[30] Aa. Vv. *Computational Theories and their Implementation in the Brain*. Oxford University Press, nov 2016.

[31] Egidio D'Angelo. The Organization of Plasticity in the Cerebellar Cortex: From Synapses to Control. *Progress in Brain Research*, 210:31–58, 2014.

[32] C Hansel, D J Linden, and E D'Angelo. Beyond parallel fiber LTD: the diversity of synaptic and non-synaptic plasticity in the cerebellum. *Nature neuroscience*, 4(5):467–475, 2001.

[33] Egidio D'Angelo, Giovanna De Filippi, Paola Rossi, and Vanni Taglietti. Ionic Mechanism of Electroresponsiveness in Cerebellar Granule Cells Implicates the

Action of a Persistent Sodium Current. *Journal of Neurophysiology*, 80(2):493–503, 1998.

[34] Alexei Kirischuk S, Verkhratsky. [Ca^(2+)]_i recordings from neural cells in acutely isolated cerebellar slices employing differential loading of membrane permeant form of calcium indicator fura-2 [Ca^(2+)]_i recordings from neural cells in acutely isolated cerebellar slices employing d. *Journal of Physiology*, (October), 1996.

[35] Rafael Yuste, Jason MacLean, Joshua Vogelstein, and Liam Paninski. Imaging action potentials with calcium indicators. *Cold Spring Harbor Protocols*, 6(8):985–989, 2011.

[36] Hecht. *Hecht E., Zajac – Optics (4th Ed., 2003).pdf*.

[37] Klein M. V. *Optics*. Second edition.

[38] Hamamatsu. LCOS-SLM (Liquid Crystal on Silicon - Spatial Light Modulator). pages 1–7. 2012.

[39] R W Gerchberg and W O Saxton. A practical algorithm for the determination of phase from image and diffraction plane pictures. *Optik*, 35(2):237–246, 1972.

[40] Jennifer E Curtis, Brian A Koss, and David G Grier. Dynamic holographic optical tweezers. *Optics Communications*, 207(June):169–175, 2002.

[41] D L Wokosin, C M Loughrey, and G L Smith. Characterization of a range of fura dyes with two-photon excitation. *Biophysical journal*, 86(3):1726–1738, 2004.

[42] Jennifer M Wilson, Daniel A Dombeck, Manuel Díaz-Ríos, Ronald M Harris-Warrick, and Robert M Brownstone. Two-photon calcium imaging of network activity in XFP-expressing neurons in the mouse. *Journal of neurophysiology*, 97(4):3118–3125, apr 2007.

[43] Lia Forti, Elisabetta Cesana, Jonathan Mapelli, and Egidio D'Angelo. Ionic mechanisms of autorhythmic firing in rat cerebellar Golgi cells. *The Journal of physiology*, 574(Pt 3):711–29, 2006.

[44] E L Bienenstock, L N Cooper, and P W Munro. Theory for the development of neuron selectivity: orientation specificity and binocular interaction in visual cortex. *The Journal of neuroscience : the official journal of the Society for Neuroscience*, 2(1):32–48, 1982.

[45] E Courchesne and G Allen. Prediction and preparation, fundamental functions of the cerebellum. *Learning & memory (Cold Spring Harbor, N.Y.)*, 4(1):1–35, 1997.

[46] Sylco S. Hoppenbrouwers, Dennis J.L.G. Schutter, Paul B. Fitzgerald, Robert Chen, and Zafiris J. Daskalakis. The role of the cerebellum in the pathophysiology and treatment of neuropsychiatric disorders: a review. *Brain Res Rev*, 59(1):185–200, 2008.

[47] J. Giza, M. J. Urbanski, F. Prestori, B. Bandyopadhyay, A. Yam, V. Friedrich, K. Kelley, E. D'Angelo, and M. Goldfarb. Behavioral and Cerebellar Transmission Deficits in Mice Lacking the Autism-Linked Gene Islet Brain-2. *Journal of Neuroscience*, 30(44):14805–14816, 2010.

[48] E D'Angelo, Thierry Nieus, Arianna Maffei, Simona Armano, Paola Rossi, Vanni Taglietti, Andrea Fontana, Giovanni Naldi, and Egidio D Angelo. Theta-frequency bursting and resonance in cerebellar granule cells: experimental evidence and modeling of a slow k+-dependent mechanism. *J Neurosci*, 21(3):759–770, 2001.

[49] Thierry Nieus, Elisabetta Sola, Jonathan Mapelli, Elena Saftenku, Paola Rossi, and Egidio D'Angelo. LTP regulates burst initiation and frequency at mossy fiber-granule cell synapses of rat cerebellum: experimental observations and theoretical predictions. *Journal of neurophysiology*, 95(2):686–99, 2006.

[50] Thierry R Nieus, Lisa Mapelli, and Egidio D'Angelo. Regulation of output spike patterns by phasic inhibition in cerebellar granule cells. *Frontiers in cellular neuroscience*, 8(August):246, 2014.

[51] Diwakar S., Magistretti J., Goldfarb M., G. Naldi, and D'Angelo E. Axonal Na+ Channels Ensure Fast Spike Activation and Back-Propagation in Cerebellar Granule Cells. *Journal of neurophysiology*, 101(2):519–532, 2009.

[52] Diwakar S. Lombardo P., Solinas S., Naldi G. and D'Angelo E. Local field potential modeling predicts dense activation in cerebellar granule cells clusters under LTP and LTD control. *PLoS ONE*, 6(7), 2011.

[53] Sergio Solinas, Lia Forti, Elisabetta Cesana, Jonathan Mapelli, Erik De Schutter, and Egidio D'Angelo. Fast-reset of pacemaking and theta-frequency resonance patterns in cerebellar golgi cells: simulations of their impact in vivo. *Frontiers in cellular neuroscience*, 1(December 2007):4, 2007.

[54] Sergio Solinas, Lia Forti, Elisabetta Cesana, Jonathan Mapelli, Erik De Schutter, and Egidio D'Angelo. Computational reconstruction of pacemaking and intrinsic electroresponsiveness in cerebellar Golgi cells. *Frontiers in cellular neuroscience*, 1(December):2, 2007.

[55] Sergio Solinas, Thierry Nieus, and Egidio D'Angelo. A realistic large-scale model of the cerebellum granular layer predicts circuit spatio-temporal filtering properties. *Frontiers in cellular neuroscience*, 4(May):12, 2010.

[56] Volodymyr Nikolenko, Kira E Poskanzer, and Rafael Yuste. Two-photon photostimulation and imaging of neural circuits. *Nature methods*, 4(11):943–950, 2007.

[57] Konnerth A. Grienberger C. Imaging Calcium in Neurons. *Neuron*, 73(5), 2012.

[58] Paola Rossi, Egidio D'Angelo, Jacopo Magistretti, Mauro Toselli, and Vanni Taglietti. Age-dependent expression of high-voltage activated calcium currents

during cerebellar granule cell development in situ. *European Journal of Physiology*, 429(1):107–116, 1994.

[59] Goldin S.M. Finch E.A., Turner T.J. Calcium as a Coagonist of Inositol 1,4,5-Trisphosphate-Induced Calcium Release. *Science*, 252(5004):443–446, 1991.

[60] AJ Irving, Graham L Collingridge, and J George Schofield. Interactions between Ca2+ mobilizing mechanisms in cultured rat cerebellar granule cells. *Journal of Physiology*, 456:667–680, 1992.

[61] Paola Rossi. Differential long-lasting potentiation of the NMDA and non-NMDA synaptic currents induced by metabotropic and NMDA receptor coactivation in cerebellar granule cells. *European Journal of Neuroscience*, 8(6):1182–1189, 1996.

[62] Arianna Maffei, Francesca Prestori, Paola Rossi, Vanni Taglietti, and Egidio D'Angelo. Presynaptic current changes at the mossy fiber-granule cell synapse of cerebellum during LTP. *Journal of neurophysiology*, 88:627–638, 2002.

[63] Traynelis F. Silver R.A. and Cull-Candy S.G. Rapid-time-course miniature and evoked excitatory currents at cerebellar synapses in situ. *Nature*, 360:40–46, 1992.

[64] Taglietti V. D'Angelo E., Rossi P. Different proportions of N-Methyl-D-Aspartate and NON-N-Methyl-D-Aspartate receptor currents at the mossy fibre-granule cell synapse of developing rat cerebellum. *Neuroscience*, 53(1):121–130, 1993.

[65] Egidio DAngelo, Giovanna De Filippi, Paola Rossi, Vanni Taglietti, Fisiologia Generale, and Via Forlanini. Synaptic excitation of individual rat cerebellar granule cells in situ : evidence for the role of NMDA receptors. *Journal of Physiology*, 484(2):397–413, 1995.

[66] L M Mehlmann, K Mikoshiba, and D Kline. Redistribution and increase in cortical inositol 1,4,5-trisphosphate receptors after meiotic maturation of the mouse oocyte. *Developmental biology*, 180(2):489–498, 1996.

[67] Dmitri Lim, Emanuela Ercolano, Keiichiro Kyozuka, Gilda A. Nusco, Francesco Moccia, Klaus Lange, and Luigia Santella. The M-phase-promoting Factor Modulates the Sensitivity of the Ca 2+ Stores to Inositol 1,4,5-Trisphosphate via the Actin Cytoskeleton. *Journal of Biological Chemistry*, 278(43):42505–42514, 2003.

[68] Zhe Xu, Carmen J. Williams, Gregory S. Kopf, and Richard M. Schultz. Maturation-associated increase in IP3 receptor type 1: Role in conferring increased IP3 sensitivity and Ca2+ oscillatory behavior in mouse eggs. *Developmental Biology*, 254(2):163–171, 2003.

[69] Michael J. Berridge. Neuronal Signalling. In *Cell Signaling Biology*, pages 1–91. 2009.

[70] David Philipona and Olivier J M D Coenen. Model of granular layer encoding in the cerebellum. *Neurocomputing*, 58-60(September 2016):575–580, 2004.

[71] Adam M Packer, Darcy S Peterka, Jan J Hirtz, Rohit Prakash, Karl Deisseroth, and Rafael Yuste. Two-photon optogenetics of dendritic spines and neural circuits. *Nature Methods*, 9(12):1202–1205, 2012.

[72] Weijian Yang, Jae eun Kang Miller, Luis Carrillo-Reid, Eftychios Pnevmatikakis, Liam Paninski, Rafael Yuste, and Darcy S. Peterka. Simultaneous Multi-plane Imaging of Neural Circuits. *Neuron*, 89(2):284, 2016.

[73] Joseph R. Lakowicz. *Principles of Fluorescence Spectroscopy*. 2006.

[74] W Denk, J H Strickler, and W W Webb. Two-photon laser scanning fluorescence microscopy. *Science (New York, N.Y.)*, 248(4951):73–76, 1990.

[75] S Mulligan and B MacVicar. Two-photon fluorescence microscopy: basic principles, advantages and risks. *Modern Research and Educational Topics in Microscopy*, pages 881–888, 2007.

[76] Michael Rubart. Two-photon microscopy of cells and tissue. *Circulation Research*, 95(12):1154–1166, 2004.

[77] Karel Svoboda and Ryohei Yasuda. Principles of Two-Photon Excitation Microscopy and Its Applications to Neuroscience. *Neuron*, 50(6):823–839, 2006.

[78] Alberto Diaspro, Giuseppe Chirico, and Maddalena Collini. Two-photon fluorescence excitation and related techniques in biological microscopy. *Quarterly reviews of biophysics*, 38(2):97–166, 2005.

[79] Peter T. C. So, Chen Y. Dong, Barry R. Masters, and Keith M. Berland. Two-Photon Excitation Fluorescence Microscopy. *Annual Review of Biomedical Engineering*, 2(1):399–429, aug 2000.

[80] Barry R. Masters and Peter T. C. So. *Handbook of biomedical nonlinear optical microscopy*. Oxford University Press, 2008.

[81] Frederik J Geurts, Erik De Schutter, and Stéphane Dieudonné. Unraveling the cerebellar cortex: cytology and cellular physiology of large-sized interneurons in the granular layer. *Cerebellum (London, England)*, 2(4):290–299, dec 2003.

[82] Henrik Jörntell, Fredrik Bengtsson, Martijn Schonewille, and Chris I. De Zeeuw. Cerebellar molecular layer interneurons - computational properties and roles in learning. *Trends in Neurosciences*, 33(11):524–535, 2010.

[83] By Susan Standring. *Gray ' s Anatomy , 40th Edition*. 2008.

[84] D B Jaffe and T H Brown. Metabotropic glutamate receptor activation induces calcium waves within hippocampal dendrites. *Journal of neurophysiology*, 72(1), 1994.

[85] Kato K. Nishiyama M., Hong K., Mikoshiba K., Poo M. Calcium stores regulate the polarity and input specifcity of synaptic modifcation. *Nature*, 408:584–588, 2000.

[86] Prestori. *Calcium dynamics at the cerebellar mossy fibre-granule cell synapse*. PhD thesis, 2004.

[87] Lin Tian, S. Andrew Hires, and Loren L. Looger. Imaging neuronal activity with genetically encoded calcium indicators. *Cold Spring Harbor Protocols*, 7(6):647–656, jun 2012.

[88] Md. Shahidul (Ed.) Islam. *Calcium signaling*. 2015.